The three-dimensional evolution of a plane mixing layer: pairing and transition to turbulence

By ROBERT D. MOSER AND MICHAEL M. ROGERS
NASA-Ames Research Center, Moffett Field, CA 94035, USA

(Received 6 March 1992 and in revised form 3 September 1992)

The evolution of three-dimensional temporally evolving plane mixing layers through as many as three pairings has been simulated numerically. All simulations were begun from a few low-wavenumber disturbances, usually derived from linear stability theory, in addition to the mean velocity. Three-dimensional perturbations were used with amplitudes ranging from infinitesimal to large enough to trigger a rapid transition to turbulence. Pairing is found to inhibit the growth of infinitesimal three-dimensional disturbances, and to trigger the transition to turbulence in highly three-dimensional flows. The mechanisms responsible for the growth of three-dimensionality and onset of transition to turbulence are described. The transition to turbulence is accompanied by the formation of thin sheets of spanwise vorticity, which undergo secondary rollups. The post-transitional simulated flow fields exhibit many properties characteristic of turbulent flows.

1. Introduction

Free shear layers are of great technological importance because they occur in many practical devices, especially those involving chemical reactions. However, a thorough understanding of the hydrodynamics of free shear flows is a prerequisite to understanding the physical processes involved in such chemically reacting systems. In Rogers & Moser (1992) (hereafter referred to as RM) and in this paper we attempt to develop such an understanding in the case of the simplest free shear flow, the plane mixing layer. Despite the fact that this flow has been extensively studied by analytical, numerical and experimental means, many questions remain unanswered. In particular, not enough is known about the development of three-dimensionality and the transition to turbulence. Here numerically simulated temporally evolving free shear layers that undergo up to three pairings of the primary Kelvin–Helmholtz rollers are examined to study these issues.

The spanwise vortices (rollers) that result from the Kelvin–Helmholtz instability of the plane mixing layer are unstable to subharmonic disturbances (Kelly 1967; Pierrehumbert & Widnall 1982). This results in the pairing of the rollers (i.e. corotation and amalgamation of neighbouring rollers). Such pairings have been observed in a variety of experimental and computational studies of the mixing layer (e.g. Winant & Browand 1974; Brown & Roshko 1974; Riley & Metcalfe 1980; Ho & Huerre 1984; Corcos & Sherman 1984; Metcalfe *et al.* 1987). Pairing can occur in two-dimensional mixing layers or in fully turbulent mixing layers. The results of Winant & Browand (1974) suggest that pairing is the primary mechanism for the growth of the layer thickness, though this may not be the case in strongly turbulent mixing layers (Hernan & Jimenez 1982). Moore & Saffman (1975) proposed a

different mechanism by which rollers can amalgamate ('tearing' or 'shredding') and this has been observed both computationally and experimentally (e.g. Riley & Metcalfe 1980; Yang & Karlsson 1991). However, tearing occurs only for a narrow range of relative phasings of the fundamental and subharmonic disturbances (Monkewitz 1988) and is therefore less likely in unforced mixing layers (Hernan & Jimenez 1982). Further, amalgamation of more than two rollers ('triplings', 'quadruplings' etc.) can occur, although this is less likely in the absence of forcing (Brown & Roshko 1974; Hernan & Jimenez 1982).

The rollers are also unstable to three-dimensional disturbances (Pierrehumbert & Widnall 1982; Corcos & Lin 1984), but this instability is apparently weakened by pairings (Metcalfe *et al.* 1987; Huang & Ho 1990). In addition to deforming the rollers (Pierrehumbert & Widnall 1982), the three-dimensional instability leads to arrays of counter-rotating 'rib' vortices, which reside in the braid region between the rollers and extend from the bottom of one roller to the top of the next (Corcos & Lin 1984; RM). If the rib vortices are sufficiently strong (i.e. have large enough circulation), then they collapse into compact nearly circular vortices, which are easily detected by flow visualization (Lin & Corcos 1984; RM). Such rib vortices have been observed in many experimental and computational studies of the mixing layer (e.g. Brown & Roshko 1974; Konrad 1976; Bernal 1981; Breidenthal 1981; Jimenez 1983; Bernal & Roshko 1986; Metcalfe *et al.* 1987; Buell & Mansour 1989). The spanwise wavelength at which the ribs form is highly variable (Lasheras & Choi 1988). However, many experiments (e.g. Huang & Ho 1990) and the analysis of Pierrehumbert & Widnall (1982) suggest that there is a preferred wavelength of roughly two-thirds of the spacing between the rollers. This spanwise lengthscale may change as the mixing layer pairs (Huang & Ho 1990), but such changes appear to be slow (Bernal & Roshko 1986; Rogers & Moser 1993).

As the mixing layer becomes more three-dimensional, it eventually undergoes a transition to turbulence (Koochesfahani & Dimotakis 1986). This transition is accompanied by a marked increase in the degree of scalar mixing in the flow, particularly at high Schmidt number (Konrad 1976; Breidenthal 1981). Because the effect on mixing is so large, this transition has been called the 'mixing transition'. In experiments, this transition occurs at Reynolds numbers (based on visual thickness and velocity difference) between 5600 and 17000 (Koochesfahani & Dimotakis 1986). Huang & Ho (1990) found that the transition was apparently linked to pairings, and that transition was completed by the second pairing. This is consistent with observations by Winant & Browand (1974). The actual mechanism of the transition has been a matter of some speculation, with Lin & Corcos (1984) proposing the collapse of the rib vortices as the initiating process and Lasheras, Cho & Maxworthy (1986) suggesting a higher-order instability. Moser & Rogers (1991) recently identified a pairing-initiated transition mechanism.

There are several unanswered questions regarding the development of three-dimensionality and the transition to turbulence in pairing mixing layers, and this study was undertaken to address some of these questions. In particular, the character of the three-dimensional instability and its inhibition by pairing is investigated. Also studied are the nonlinear evolution of three-dimensional disturbances during pairings, including transition mechanisms. Finally, characteristics of the post-transitional turbulent flows are of interest. These issues are addressed using direct numerical simulation of mixing layers undergoing multiple pairings (up to three) at large Reynolds numbers (up 10000 based on visual thickness and velocity difference).

Some of the discussion in the following section relies on results and definitions from the first portion of this study (RM), which deals with the rollup of three-dimensional mixing layers. A review of the necessary material appears in the Appendix. Also, a brief description of some aspects of the small-scale transition discussed here appeared in Moser & Rogers (1991).

In §2, background information on the numerical simulations used in this study is presented. Some important results from two-dimensional pairing simulations are given in §3. Linear stability of the pairing two-dimensional mixing layer is discussed in §4, and nonlinear evolutions of flows undergoing one and two pairings are presented in §§5 and 6, respectively. Finally, the characteristics of the post-transitional 'turbulent' flows are described in §7 and a summary is given in §8.

2. Preliminaries

The results presented in this study are obtained by examining direct numerical simulations of time-developing mixing layers. A time-developing formulation was used because it makes possible the simulation of the higher Reynolds numbers required for the study of transition to turbulence. The evolution of vorticity structure in spatially developing mixing layers is expected to be similar (Buell, Moser & Rogers 1992).

As in RM, the flows described here were initialized with simple 'clean' initial conditions (see §2.2) with relatively short spanwise wavelengths. This results in the 'standard' rib and roller structures observed in experimental mixing layers. The absence of broadband initial disturbances permits the study of transition to turbulence from an organized flow.

2.1. *The governing equations and numerical considerations*

The simulations reported here were performed by solving the vorticity equation derived from the incompressible Navier–Stokes equations:

$$\frac{\partial \boldsymbol{\omega}}{\partial t} + \boldsymbol{\nabla} \times (\boldsymbol{\omega} \times \boldsymbol{U}) = \frac{1}{Re_0} \nabla^2 \boldsymbol{\omega}, \tag{1}$$

where $\boldsymbol{U}(x, y, z, t)$ is the velocity vector (with components u, v and w), and $\boldsymbol{\omega} \equiv \boldsymbol{\nabla} \times \boldsymbol{U}$ is the vorticity vector. Here, U (the half-velocity difference) and δ_ω^0 (the initial vorticity thickness of the layer, see equation (4)) have been used to non-dimensionalize the equations and form the Reynolds number $Re_0 = U\delta_\omega^0/\nu$ (ν is the kinematic viscosity). This non-dimensionalization is used throughout the paper. In addition, the evolution of a passive scalar T is computed using the scalar equation

$$\frac{\partial T}{\partial t} + \boldsymbol{U} \cdot \boldsymbol{\nabla} T = \frac{1}{Pe_0} \nabla^2 T, \tag{2}$$

where the Péclet number is given by $Pe_0 = Re_0 Sc$ and the Schmidt number is $Sc = \nu/\gamma$ (γ being the molecular diffusivity of the scalar).

The above equations are solved using periodic boundary conditions with periods L_x and L_z in the streamwise (x) and spanwise (z) spatial directions and an infinite domain in the cross-stream (y) direction. The pseudospectral numerical method used is described in detail in Spalart, Moser & Rogers (1991). As many as $192 \times 212 \times 128$ Fourier/Jacobi modes and 380 hours on a Cray Y-MP were required to simulate the turbulent flows described in §7 (e.g. TURB2P).

2.2. *Specification of initial conditions*

The initial mean velocity and passive scalar profiles used for all the simulations reported here are of the form

$$\bar{U} = U \operatorname{erf}(\pi^{\frac{1}{2}} y/\delta_\omega^0), \quad \bar{T} = \tfrac{1}{2}(1 + \operatorname{erf}(\pi^{\frac{1}{2}} y/\delta_\omega^0)). \tag{3}$$

Note that the velocity profile has a vorticity thickness of δ_ω^0, where the vorticity thickness is

$$\delta_\omega \equiv \frac{2U}{(\partial \bar{U}/\partial y)|_{\max}}. \tag{4}$$

In addition to the mean velocity, simple perturbations are included in the initial conditions. These perturbations include just one or a few of the x- and z-Fourier modes of the representation. Streamwise and spanwise fundamental wavelengths (λ_x and λ_z) are chosen to be the most unstable wavelengths from linear theory ($\lambda_x = 2.32\pi$, see Monkewitz & Huerre 1982, and $\lambda_z = 0.6\lambda_x$, see Pierrehumbert & Widnall 1982; Rogers & Moser 1993) and perturbations with these wavelengths and their subharmonics are used in the initial conditions. To accommodate these perturbations, the computational domain must be an integer multiple of the wavelengths in the x- and z-directions. Thus, in general, $L_x = N\lambda_x$ and $L_z = M\lambda_z$. To accommodate the subharmonic disturbances for the cases reported here, N and M are as large as 8.

To specify the initial conditions and facilitate discussion throughout this paper, it is necessary to refer to specific wavenumbers; they will be referred to in ordered pairs

$$(\alpha, \beta) = \left(\frac{k_x \lambda_x}{2\pi}, \frac{k_z \lambda_z}{2\pi}\right), \tag{5}$$

where k_x and k_z are the x and z wavenumbers respectively. Thus the fundamental modes discussed above have α and/or β equal to one. Note that because the quantities under consideration are real, the Fourier coefficients of the (α, β) and the $(-\alpha, -\beta)$ modes are complex conjugates (denoted by $\dagger$). Thus only modes with $\alpha \geqslant 0$ need to be considered here.

The amplitude of a given Fourier mode (of an initial perturbation or in the evolved field) can be measured by the integrated (in y) r.m.s. velocity of the mode. Thus we define

$$A_{\alpha\beta} = \begin{cases} \left[\int_{-\infty}^{+\infty} 2\hat{u}_i(\alpha,\beta)\,\hat{u}_i^\dagger(\alpha,\beta)\,\mathrm{d}y\right]^{\frac{1}{2}} & \text{if} \quad \alpha = 0 \quad \text{or} \quad \beta = 0; \\ \left[\int_{-\infty}^{+\infty} 2[\hat{u}_i(\alpha,\beta)\,\hat{u}_i^\dagger(\alpha,\beta) + \hat{u}_i(\alpha,-\beta)\,\hat{u}_i^\dagger(\alpha,-\beta)]\,\mathrm{d}y\right]^{\frac{1}{2}} & \text{otherwise.} \end{cases} \tag{6}$$

Here $\hat{u}_i(\alpha, \beta)$ is the (α, β) Fourier coefficient of the velocity component u_i. Note that $A_{\alpha\beta}$ is only defined for non-negative α and β since it includes the contributions of all the $(\pm\alpha, \pm\beta)$ modes. The amplitude associated with all modes with a particular spanwise wavenumber and the amplitude of all three-dimensional Fourier modes ($\beta \neq 0$) are also of interest. They are denoted by $A_{s\beta}$ and A_{3D} respectively (the subscript s signifies a sum over streamwise wavenumbers α), and are defined

$$A_{s\beta} = \left[\sum_{J=0}^{N_x/2-1} (A_{J\beta})^2\right]^{\frac{1}{2}}, \qquad A_{3D} = \left[\sum_{J=1}^{N_x/2-1} (A_{sJ})^2\right]^{\frac{1}{2}}. \tag{7}$$

Note, that as a special case, A_{s0} is the amplitude associated with all two-dimensional modes. Throughout this paper, $A_{\alpha\beta}$, $A_{s\beta}$ and A_{3D} are quoted normalized by $U(\delta_\omega^0)^{\frac{1}{2}}$. A

superscript 0 (e.g. $A^0_{\alpha\beta}$) will be used to denote the amplitude at $t = 0$ and a superscript $*$ will indicate the amplitude normalized by its value at $t = 0$ (e.g. $A^*_{\alpha\beta} = A_{\alpha\beta}/A^0_{\alpha\beta}$).

All the simulations reported here were initialized with two-dimensional spanwise vorticity perturbations, which lead to the Kelvin–Helmholtz rollup and subsequent pairings of the mixing layer. The spanwise vorticity perturbation has the form

$$\omega_z = \sum_{\alpha=1,\frac{1}{2},\frac{1}{4}\ldots} A^0_{\alpha 0}\,\mathrm{Re}\,(f_\alpha(y)\,\mathrm{e}^{\mathrm{i}(k_x x-\phi_{\alpha 0})}), \tag{8}$$

where Re signifies the real part of a complex argument. In most cases the complex functions $f_\alpha(y)$ are the stability eigenfunctions for the vorticity, determined from the Orr–Sommerfeld equation for that wavenumber. Each eigenfunction is normalized such that its integrated energy is one, its real part is symmetric in y (and positive at $y = 0$) and its imaginary part is antisymmetric. In some cases $f_\alpha(y)$ was chosen to be a Gaussian ($f_\alpha(y) = c_\alpha \mathrm{e}^{-\pi y^2}$, where c_α is a normalization constant chosen such that the integrated energy in the $(\alpha, 0)$ mode is unity when $A_{\alpha 0}$ is one), which is referred to as an ω-Gaussian initial condition. The phase ϕ_{10} is irrelevant to the evolution of the flow, and is set to zero for convenience. The phases $\phi_{\alpha 0}$ of the subharmonics ($\alpha = \frac{1}{2}$, $\frac{1}{4}$ etc.) relative to the fundamental ($\alpha = 1$) determine whether large-scale amalgamations occur by pairing or tearing (see Riley & Metcalfe 1980; Monkewitz 1988). In all cases the optimum pairing phase ($\phi_{\alpha 0} = 0$) was selected. The amplitudes $A^0_{\alpha 0}$ vary depending on α and the case being considered. They are reported for each case in the relevant sections.

As in RM, three-dimensionality was introduced in the simulations by including initial perturbations in the $(0, \pm\beta)$ modes. These are referred to as streamwise invariant disturbances. For these modes, only the streamwise vorticity component is made non-zero and the following functional form is used:

$$\omega_x = \sum_{\beta=1,\frac{1}{2},\frac{1}{4}\ldots} A^0_{0\beta} g_\beta(y) \sin\,(k_z z - \phi_{0\beta}). \tag{9}$$

The function $g_\beta(y)$ is either an ω-Gaussian disturbance ($g_\beta(y) = c_\beta \mathrm{e}^{-\pi y^2}$) or is such that the vertical velocity v is a Gaussian (v-Gaussian disturbance, $g_\beta(y) = c_\beta(4y^2 - 2 - k_z^2)\,\mathrm{e}^{-y^2}/k_z$). In either case, c_β is a normalization constant selected such that the integrated energy in the $(0, \beta)$ mode is unity when $A_{0\beta}$ is one. An eigenfunction is not used for this mode because there are no eigenfunctions satisfying the boundary conditions. The phase ϕ_{01} is irrelevant to the flow evolution and for convenience is set to zero. The subharmonic phases *are* important and the effect of varying them is discussed in Rogers & Moser (1993). In Rogers & Moser (1991) it was shown that the flow evolution resulting from the streamwise-invariant disturbances used here is typical of the evolutions resulting from a variety of other three-dimensional disturbances.

2.3. *Flow symmetries*

In some cases, the initial conditions (8) and (9) described in §2.2 possess two spatial symmetries that are preserved by the Navier–Stokes equations. Whether or not these symmetries exist depends on the spanwise subharmonics and their phases ($\phi_{0\beta}$). One possible symmetry is a z-plane reflection symmetry,

$$\left.\begin{aligned} &\omega_i(x, y, z) = -\omega_i(x, y, -z + 2z_s), \quad \text{where} \quad i = x \quad \text{or} \quad y, \\ &\omega_z(x, y, z) = \omega_z(x, y, -z + 2z_s), \end{aligned}\right\} \tag{10}$$

where $z = z_s$ is a symmetry plane. If this symmetry exists, there are two such

Simulation	A_{10} $\times 10^2$	$A_{\frac{1}{2}0}$ $\times 10^2$	$A_{\frac{1}{4}0}$ $\times 10^2$	$A_{\frac{1}{8}0}$ $\times 10^2$	τ_r	τ_{o0}	τ_{p1}	τ_{s1}	τ_{o1}	τ_{p2}	τ_{s2}	τ_{o2}	τ_{p3}	τ_{s3}
2D0P	4.00	—	—	—	13.4	17.5	—	—	—	—	—	—	—	—
2D1P	4.00	3.00	—	—	11.9	—	21.5	29.2	46.5	—	—	—	—	—
2D2P	4.00	3.00	3.00	—	11.9	—	21.5	31.2	—	46.7	63.9	90.3	—	—
2D3P	4.00	3.00	3.00	3.00	11.9	—	21.5	32.0	—	47.0	66.7	—	103.7	139.8
2D1PDEL	4.00	1.00	—	—	13.1	20.0	26.4	34.4	—	—	—	—	—	—
2D2PωG	$4.52^{\omega G}$	$3.47^{\omega G}$	$5.14^{\omega G}$	—	11.8	—	21.0	35.3	—	39.9	60.7	—	—	—

TABLE 1. Parameters of the two-dimensional simulations. Disturbance profiles are eigenfunctions except for 2D2PωG, in which they are ω-Gaussian (indicated by $^{\omega G}$). $Re_0 = 250$, $\phi_{\alpha 0} = 0$, $Pr = 1.0$ and $\lambda_x = 1.16(2\pi)$ for all cases. 2D3P was not run long enough to determine τ_{o3}, 2D1PDEL was not run long enough to determine τ_{o1}, and 2D2PωG was not run long enough to determine τ_{o2}.

symmetry planes in the domain, located at $z = 0$ and $z = \frac{1}{2}L_z$ for the initial condition in (9). Note that both ω_x and ω_y are zero in these symmetry planes. The other possible symmetry is a point-reflection symmetry,

$$\omega_i(x, y, z) = \omega_i(-x + 2x_s, -y, -z + 2z_s), \tag{11}$$

where $(x, y, z) = (x_s, 0, z_s)$ is a symmetry point. If this symmetry is present, there are four such symmetry points in the domain, located at $(0, 0, \frac{1}{4}\lambda_z)$, $(0, 0, \frac{1}{2}L_z + \frac{1}{4}\lambda_z)$, $(\frac{1}{2}L_x, 0, \frac{1}{4}\lambda_z)$, and $(\frac{1}{2}L_x, 0, \frac{1}{2}L_z + \frac{1}{4}\lambda_z)$ for the values of $\phi_{\alpha 0}$ and $\phi_{0\beta}$ used in (8) and (9).

These symmetry planes and points provide well-defined reference locations in the flow. The Kelvin–Helmholtz roller that remains after all pairings are complete is centred at $x = \frac{1}{2}L_x$ (for $\phi_{x0} = 0$), the x-location of two of the symmetry points. The braid regions between the final roller and its periodic images are centred on the other symmetry points at $x = 0$ (and by periodicity at $x = L_x$). The rib vortices that form in the surviving braid region (see RM) are centred on the $x = 0$ symmetry points.

The reference locations described above can be used to define three special planes that will be used to view the simulated flow fields (see figure 1 of RM). Two are (x, y)-planes: the between-ribs plane (BP) and the rib plane (RP). The between-ribs planes are coincident with the planes of symmetry at $z = 0$ and $z = \frac{1}{2}L_z$, and are always located between a pair of ribs. The rib planes at $z = \frac{1}{4}\lambda_z$ and $\frac{1}{2}L_z + \frac{1}{4}\lambda_z$ pass through the ribs (halfway between the BPs when $L_z = \lambda_z$) and contain the symmetry points. Note that the BP is not well defined if the plane symmetry (10) is broken and the RP is not well defined if the point symmetry (11) is broken. The other plane used here is the (z, y)-plane through the middle of the surviving braid region (the MP). Thus for the disturbances used here, the MP is located at $x = 0$ (and $x = L_x$ by periodicity). If the point-reflection symmetry exists, the MP contains two of the symmetry points.

The presence of these symmetries in the flows considered here simplifies the analysis of the simulations by allowing unambiguous definitions of the special planes discussed above as well as other items (e.g. rib circulation and rib vortex lines). Of course laboratory mixing layers do not possess these symmetries; therefore, flows that break one or both of the symmetries have been simulated to confirm that the insights gained from these idealized symmetric cases are valid in general. Indeed, flows without these symmetries evolve qualitatively like the typical symmetric flows (see §7, Rogers & Moser 1991, and Moser & Rogers 1992).

3. Two-dimensional pairings

In this section a brief description of the behaviour of two-dimensional mixing layers is given. The flows described are the time-evolving base flows for the infinitesimal three-dimensional perturbations studied in §4. The discussion here emphasizes features of two-dimensional mixing layers that have a large impact on the evolution of three-dimensionality. It is therefore essential for understanding the rest of this paper, although a few of these features have been reported previously. In addition, the flows examined here undergo up to three pairings of the spanwise Kelvin–Helmholtz rollers, which permits the study of a longer flow evolution than previously possible. A list of the two-dimensional simulations for which data are presented is given in table 1.

In the now familiar pairing process, pairs of well-developed rollers come together, corotate and eventually amalgamate. Both the number of rollers and the number of braid regions are thus halved, with the contents of every other braid region being absorbed into the new paired roller. The surviving braid region continues to be depleted of spanwise vorticity as all the vortical fluid is drawn into the paired roller. As the cores of the original spanwise rollers merge into a new, roughly circular core, spiral arms of weaker spanwise vorticity are ejected away from the paired eddy. (This is required by energy conservation, see Martel, Mora & Jimenez 1989.) The tips of these spiral arms develop a characteristic hook shape and are eventually drawn back into the surviving braid regions between the paired eddy and its periodic images. This process repeats itself after each pairing as can be seen in figure 1, where the paired rollers during and after the first, second, and third pairings are shown.

As in RM, the first maximum in time of the fundamental disturbance amplitude A_{10} is taken to define the 'rollup time', τ_r. Similarly, the first maximum of the subharmonic amplitude ($A_{\frac{1}{2}0}$) is taken to be the 'first pairing time', τ_{p1}, which is 21.5 for most cases considered here (see table 1). More generally, the nth pairing time τ_{pn} is determined by the time of the first maximum of $A_{\frac{1}{2^n}0}$. Vorticity contours at τ_{p1}, τ_{p2}, and τ_{p3} are shown in figure 1 (a, c, e). At each pairing time, the pairing rollers are in about the same relative position, indicating that the maximum in $A_{\alpha 0}$ is a consistent measure of the pairing time in these cases. It can be seen from figure 1 that at a pairing time the paired eddy is largely vertical with a short streamwise extent (the momentum thickness reaches a local maximum near the pairing time, see figure 2c). At this point, the original vortex cores have corotated by about 120°. Note that Ho & Huang (1982) use a similar definition to define the pairing location in their spatially developing layer, except that only the u-component is used to determine the mode amplitude. By this definition the pairing time occurs sooner, consistent with Ho & Huang's observation that the vortex cores have rotated by only 90° at their pairing time.

As a pairing proceeds, the streamwise lengthscale and the thickness (as measured by δ_m, see figure 2c) of the layer double. This has two important consequences. First, since the velocity scale remains the same, the timescale also doubles. For this reason the time between pairings approximately doubles with each pairing (see table 1). The second consequence is that the (surviving) mid-braid strain rate (S), is approximately halved with each pairing. This is illustrated in figure 2(b) where the mid-braid strain-rate evolutions for 2D0P, 2D1P, 2D2P, and 2D3P are plotted. Note that the late-time plateau level of S for 2D1P is about 2.5 times lower than for 2D0P (0.2 versus 0.5), but that each additional pairing does halve the plateau level (approximately 0.1 for 2D2P and 0.05 for 2D3P).

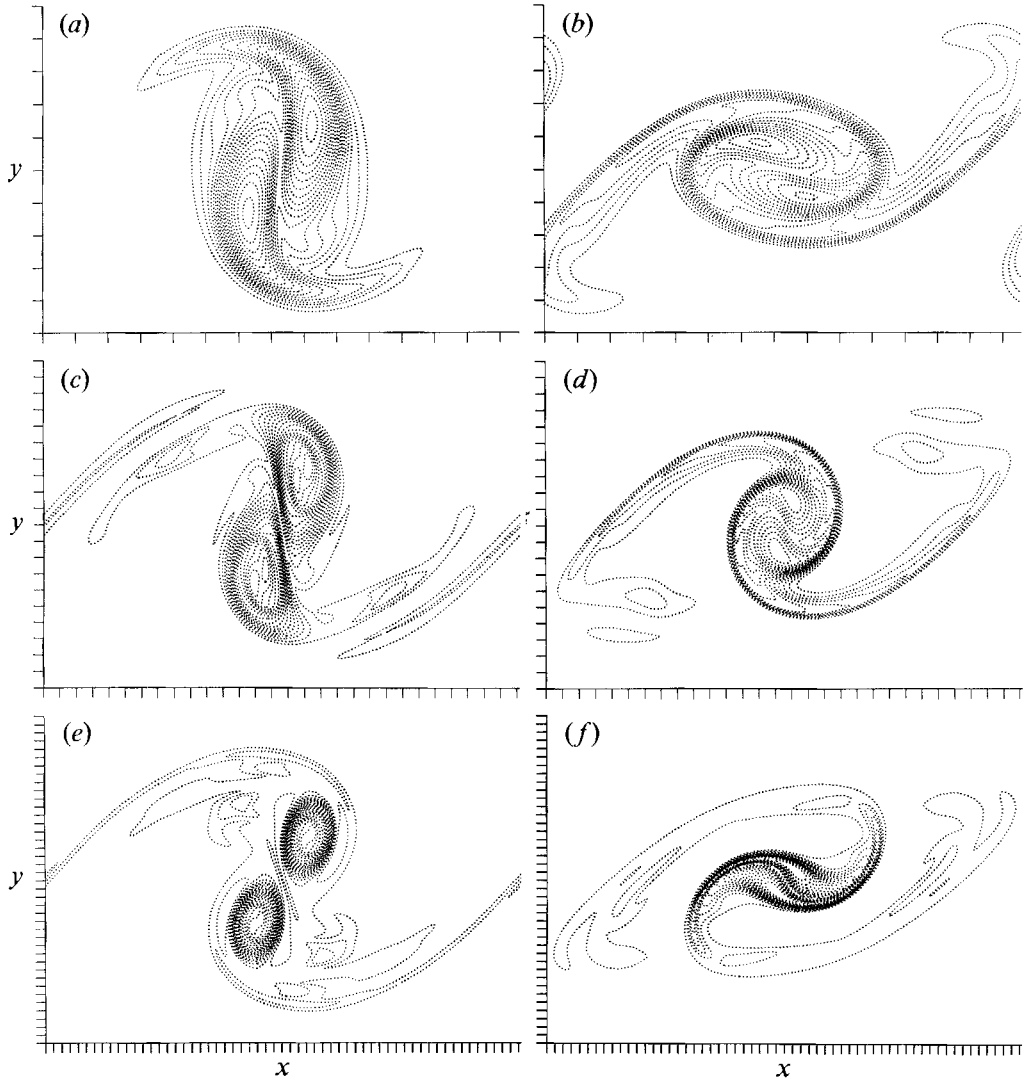

FIGURE 1. Contours of ω_z from flow 2D1P at (*a*) $t = 21.5 = \tau_{p1}$ and (*b*) $t = 30.4 \approx \tau_{s1}$, flow 2D2P at (*c*) $t = 47.5 \approx \tau_{p2}$ and (*d*) $t = 63.8 \approx \tau_{s2}$, and flow 2D3P at (*e*) $t = 104.8 \approx \tau_{p3}$ and (*f*) $t = 140.1 \approx \tau_{s3}$. The contour increment is (*a*, *b*) -0.10, (*c*, *d*) -0.08 and (*e*, *f*) -0.06. In this and subsequent similar figures dotted contours indicate negative vorticity, solid contours positive vorticity and tic marks are at δ_ω^0 increments.

In the single rollup cases discussed in RM, the roller cores eventually became elliptical and spanwise vorticity was advected into the braid region (oversaturation). This does not happen after the rollup in the pairing cases shown in figure 1 because the pairing begins before oversaturation occurs. After the pairing, however, the spiral arms discussed above bring spanwise vorticity back into the braid region. This re-entry is evident in the evolution of $-\omega_b$, shown in figure 2(*a*), where this re-entry of spanwise vorticity is marked by sudden increases in $-\omega_b$. The time at which the first such re-entry occurs is referred to as τ_{s1} (the subscript 1 signifying re-entry after the first pairing) and is 29.2 for 2D1P. Note that before the first pairing, $-\omega_b$ becomes very small (0.02 compared to about 2 at $t = 0$) and there is virtually no

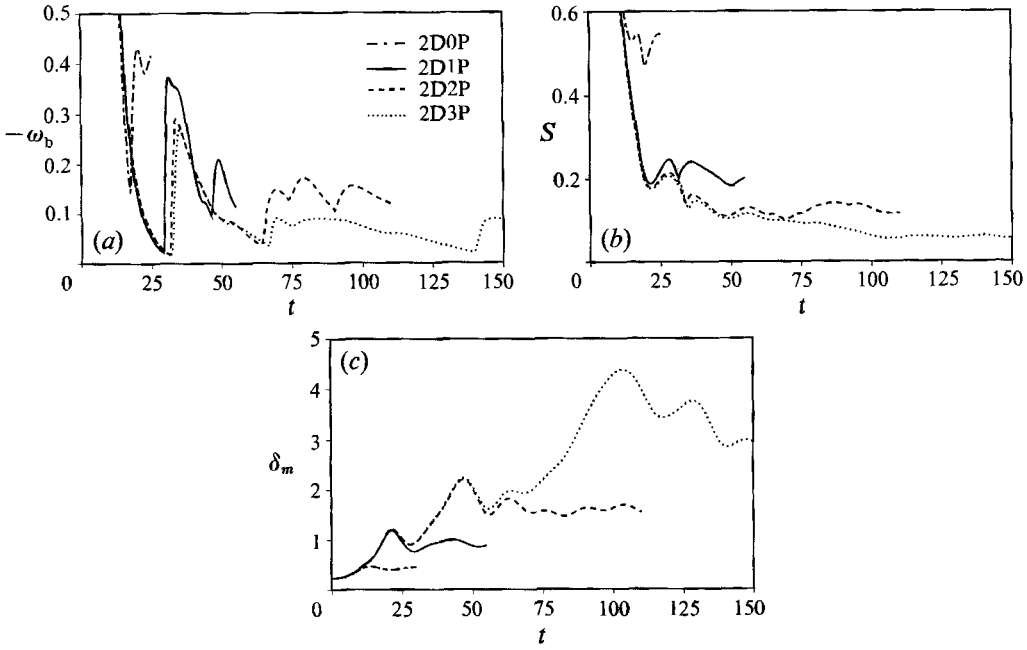

FIGURE 2. Time development of (*a*) mid-braid spanwise vorticity, (*b*) mid-braid strain rate, and (*c*) momentum thickness for 2D0P, 2D1P, 2D2P, and 2D3P.

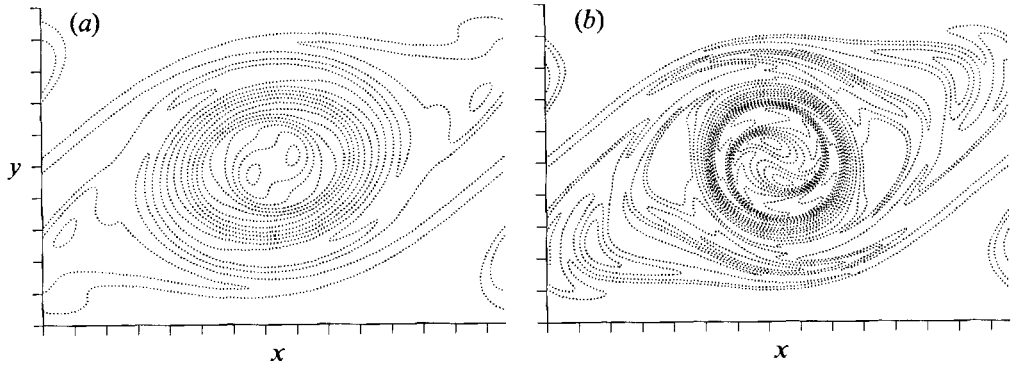

FIGURE 3. Contours of ω_z from (*a*) 2D1P at $t = 47.2 \approx \tau_{o1}$ and (*b*) a similar flow with $Re_0 = 1000$, also just after τ_{o1}. The contour increment is -0.1, with an extra contour at -0.05 to show the elliptical shape of the rollers.

vorticity left in the braid region. Similarly, τ_{sn} denotes the time at which vorticity from the spiral arms re-enters the surviving braid region after the nth pairing, where the minimum in $-\omega_b$ is used to determine its precise value. Vorticity contours at times τ_{s1}, τ_{s2}, and τ_{s3} are shown in figure 1 (*b*, *d*, *f*). Entry of the spiral arms into the braid region is apparently an inevitable consequence of pairing, as no pairing two-dimensional initial conditions have been found that lead to the suppression of this re-entry.

The vorticity $-\omega_b$ also increases abruptly another time, well after the last spiral-arm re-entry for each case (figure 2*a*). This re-entry does not occur for cases that undergo further pairings. As can be seen in figure 3, this final re-entry occurs when the paired roller becomes elliptical and is eventually advected into the braid region.

This 'oversaturation' is similar to that which occurs after the rollup in the absence of pairing. The oversaturation time is denoted by τ_{on} (see table 1), where n is the number of pairings that have occurred prior to the oversaturation.† All of the flows will eventually reach oversaturation, although the 2D3P flow was not run long enough to determine τ_{o3}. In addition to the major re-entry events associated with the spiral arms and oversaturation, there are some minor increases in $-\omega_b$ at $t \approx 75$ ($\tau_{s2} \approx 65$) and at $t \approx 151$ ($\tau_{s3} = 139.8$). These are caused by the internal structure of the spiral arms. When $Re_0 = 250$, the spiral arms resulting from the first pairing have a simpler internal structure (figure 1) and thus do not result in such secondary increases in $-\omega_b$.

The oversaturation described above is caused by the advection of vorticity into the braid region, and is not a low-Reynolds-number effect associated with viscous diffusion. Vorticity contours just after oversaturation for a single-pairing case with $Re_0 = 1000$ are shown in figure 3(*b*). The pattern is quite similar to that just after oversaturation in the 2D1P flow with $Re_0 = 250$, although the vorticity re-entering the braid region has more internal structure at the higher Reynolds number (and consequently a more complicated $-\omega_b$ evolution after τ_{o1}).

As noted above, the τ_{pn} are consistent measures of the pairing times, the rollers being in about the same relative position at each τ_{pn} (figure 1). The structure of the flow is also similar at each τ_{sn}. Despite this general similarity, there are differences among the structures at each pairing. With each additional pairing, the vorticity becomes more concentrated relative to the dominant lengthscale in the flow (i.e. the roller spacing). For a self-similar evolution, the vorticity from two rollers would have to combine and fill an area of four times the original roller area (with half the peak vorticity since the circulation is conserved). The only mechanism for spreading out the vorticity in this way is viscous diffusion, and since the Reynolds number doubles with each pairing, diffusion cannot keep pace with the pairings. The resulting paired rollers thus have high vorticity concentrated in a relatively small area (figure 1).

The details of the spiral arm structures also change between pairings. They become proportionately weaker with each pairing, and extend further around the roller. This second feature is also related to the fact that the concentrated vorticity is in a proportionately smaller area. The timescale for rotation of the concentrated core does not increase as fast as the timescale for the evolution of the spiral arms. Thus the concentrated core turns over further by the time the spiral arms cross the mid-braid plane.

Finally, with each additional pairing, there are more small-scale structures in the flow. This is expected, because the effective Reynolds number of the flow has increased. Also each pairing introduces more fine structure as the rollers move around each other (like kneading bread).

The occurrence or suppression of an oversaturation before a pairing is dependent on the timing of that pairing. In particular, if a pairing is delayed, then oversaturation can occur before the pairing begins to dominate the evolution. This occurs in 2D1PDEL, in which the initial $A_{\frac{1}{2}0}$ is 0.01 rather than 0.03 as in the standard case. The mid-braid spanwise vorticity ($-\omega_b$), the mid-braid strain rate (S), and the momentum thickness (δ_m) are shown in figure 4 for 2D1P, 2D1PDEL and 2D0P ($A_{\frac{1}{2}0} = 0$). These quantities indicate that 2D1PDEL follows the non-pairing behaviour (2D0P) longer than 2D1P. In particular, $-\omega_b$ indicates that there is a re-entry of spanwise vorticity into the braid region at $\tau_{o0} = 20.0$, before the pairing ($\tau_{p1} = 26.4$).

† The non-pairing oversaturation time, which was called τ_o in RM, will be called τ_{o0} here to avoid confusion with the postpairing oversaturations.

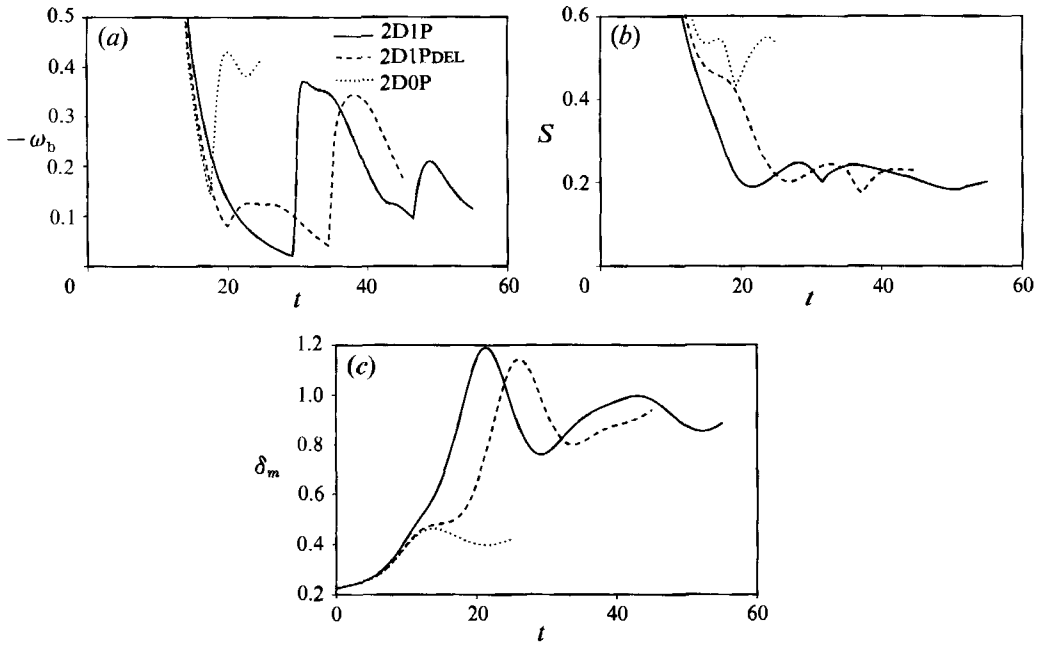

FIGURE 4. Time development of (*a*) mid-braid spanwise vorticity, (*b*) mid-braid strain rate and (*c*) momentum thickness for 2D1P, 2D1PDEL, and 2D0P.

This oversaturation is delayed somewhat compared to the non-pairing case (2D0P, $\tau_{00} = 17.5$) and the amount of vorticity re-entering the braid region is less. After the pairing, the evolution of 2D1PDEL is similar to that of 2D1P, but delayed in time.

As was done in RM, the flow structure and various flow statistics were examined for a range of Reynolds numbers, $100 \leqslant Re_0 \leqslant 1000$. The observed variations with Re_0 are similar to those presented in RM (see Moser & Rogers 1992 for details) and indicate that while significant low-Reynolds-number effects occur at $Re_0 = 100$, $Re_0 = 250$ is large enough to eliminate the worst such effects. An initial Reynolds number of 250 was therefore used for the simulations in the remainder of this paper. This marginally adequate Reynolds number was accepted because the pairing simulations are significantly more computationally intensive than the non-pairing simulations in RM, where the initial Reynolds number was chosen to be 500. One Reynolds number effect that was not discussed in RM is the presence, at $Re_0 = 500$ and $Re_0 = 1000$, of second sudden increases in $-\omega_b$ after τ_{s1}. These are due to the internal structure of the spiral arms as observed after the second and third pairings in the $Re_0 = 250$ flows.

4. Evolution of infinitesimal three-dimensional perturbations

It was seen in RM that linear analysis of the type performed by Corcos & Lin (1984) provides a good description of the three-dimensional rollup of a mixing layer. Several similar linear computations in which the base flow undergoes one or more pairings are described in this section. As in Corcos & Lin (1984), we compute the evolution of three-dimensional infinitesimal perturbations evolving in a two-dimensional mixing layer as it rolls up and pairs. Since the base flow is time-evolving, initial perturbations must be specified (there is no eigenvalue problem). Streamwise-invariant vorticity perturbations with various spanwise wavenumbers are used as discussed in §2.2.

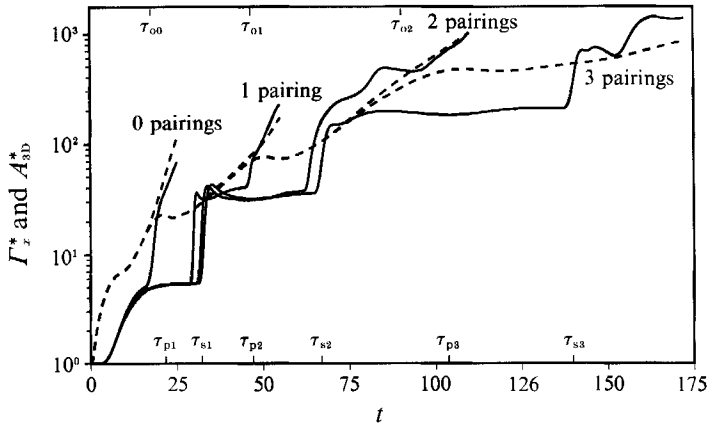

FIGURE 5. Time development of Γ_x^* (——) and A_{3D}^* ($A_{3D}^* = A_{s1}^*$) (- - - -) of three-dimensional linear perturbations with $\beta = 1$ evolving in the presence of a two-dimensional base flow that undergoes 0, 1, 2, or 3 pairings (2D0P, 2D1P, 2D2P, and 2D3P respectively).

4.1. *Growth of three-dimensional perturbations*

The two measures of the strength of the three-dimensional perturbations used here are the amplitude ($A_{3D}^* = A_{3D}/A_{3D}^0$) and the streamwise circulation in the surviving MP ($\Gamma_x^* = \Gamma_x/\Gamma_x^0$). The evolution of both these quantities for three-dimensional perturbations with $\beta = 1$ (where $\lambda_z = 0.6\lambda_x$) is shown in figure 5. Four cases, which undergo 0, 1, 2, or 3 pairings, are shown (the two-dimensional base flows are 2D0P, 2D1P, 2D2P, and 2D3P and are described in §3). Despite the differences in the details of their growth, the magnitudes of A_{3D}^* and Γ_x^* remain similar through three pairings and three orders of magnitude of growth. In particular, the agreement between A_{3D}^* and Γ_x^* after oversaturation is excellent. (Note the flow undergoing three pairings does not reach oversaturation during the time shown.) Also, neither A_{3D}^* nor Γ_x^* grow smoothly in time. Both quantities exhibit plateaux at each pairing time, with the plateaux for the circulations (solid curves) being particularly long. As explained in RM, sudden jumps in the MP circulation are caused by the re-entry of spanwise vorticity into the braid region (RM §3.1). In figure 5, there are circulation jumps for each such re-entry, that is, at each τ_{sn} and at the oversaturation time for each case. The slight variation in the timing of the circulation jumps is due to the variation in the re-entry times caused by subsequent pairings. More significant differences in the Γ_x^* evolution are apparent after oversaturation for each case. Flows undergoing further pairings do not exhibit a growth in Γ_x^* at this point (they are not oversaturated). As with Γ_x^*, there is very little difference in A_{3D}^* (dashed curves) among the cases until oversaturation, well after the last pairing of each case. Thus, by these measures, a flow becomes significantly affected by the lack of further pairings at oversaturation.

The circulation jumps that occur prior to later pairings reach the next plateau level quickly. Those that occur after the last pairing of each case are more irregular and protracted. This is because further pairings draw the vorticity in the spiral arms back out of the braid region and therefore shorten the period over which the circulation can increase. It is also apparent in figure 5 that the irregularity in the circulation jump after the final pairing of each simulation increases with the pairing number. This is due to the greater complexity of the perturbation and base flow as the number of pairings increases.

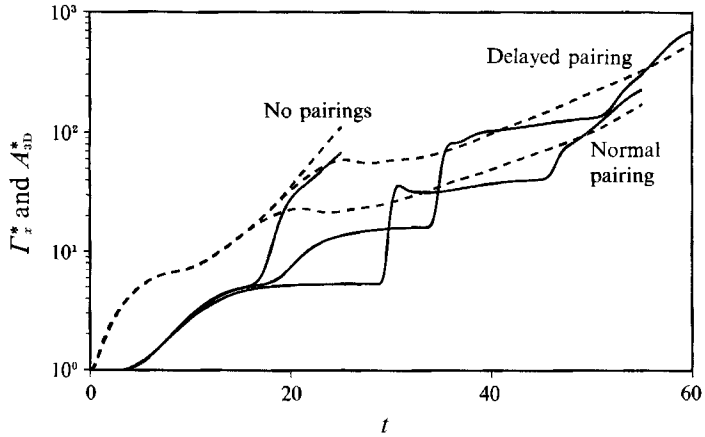

FIGURE 6. Time development of Γ_x^* (——) and A_{3D}^* ($A_{3D}^* = A_{s1}^*$) (----) of three-dimensional linear perturbations with $\beta = 1$ evolving in the presence of a two-dimensional base flow which undergoes no pairings, a delayed pairing, or a normal pairing (2D0P, 2D1PDEL, and 2D1P respectively).

At each level, further pairings result in less three-dimensional energy growth and less circulation growth than that associated with oversaturation, i.e. the A_{3D}^* and Γ_x^* curves for cases with more pairings lie below those with fewer pairings. Thus pairings inhibit the growth of three-dimensionality, although pairings do not actually reduce three-dimensionality. This has been observed both in experiments (Huang & Ho 1990) and in other numerical simulations (Metcalfe *et al.* 1987, compare E_Σ in their figure 17 to the single-pairing A_{3D}^* curve in figure 5). Pairing produces this inhibition of three-dimensionality by suppressing the oversaturation of the two-dimensional roller, thus preventing the re-entry of spanwise vorticity into the surviving braid region. Since spanwise vorticity is then essentially absent from the braid region, the rib circulation cannot grow. This limits the possible growth of three-dimensionality as discussed below. This growth limitation is only temporary since spanwise vorticity (associated with the spiral arms) does ultimately re-enter the braid region (see §3).

If pairing is significantly delayed, oversaturation can occur prior to the pairing (§3), resulting in more growth of three-dimensionality. This is illustrated in figure 6 where A_{3D}^* and Γ_x^* are shown for the non-pairing and single-pairing cases (2D0P and 2D1P) as well as the delayed-pairing case (2D1PDEL). Because the pairing is not progressing fast enough to prevent spanwise vorticity from entering the braid region, the circulation increases around $\tau_{o0} = 20.0$ in the delayed-pairing case (by a factor of 3) and there is a corresponding increase in A_{3D}^*. In the delayed-pairing case, the spiral arms form later and the corresponding jump in circulation is consequently also delayed. Interestingly, the factor by which the circulation increases at τ_{s1} is about the same in the delayed-pairing and normal-pairing cases. After τ_{o1} (the second oversaturation to occur in the delayed-pairing case) the growth of both A_{3D}^* and Γ_x^* for the pairing cases is qualitatively similar, although the level of these quantities in the delayed-pairing case is higher. The increased three-dimensionality resulting from the first oversaturation (τ_{o0}) in the delayed-pairing case is thus permanently embedded in the flow; it is not just a temporary increase until the pairing is completed.

Note that the circulation increase associated with the re-entry of vorticity into the braid region that occurs during the first oversaturation in the delayed pairing case begins somewhat before $\tau_{o0} = 20.0$. This is because the minimum in $-\omega_b$ is not a

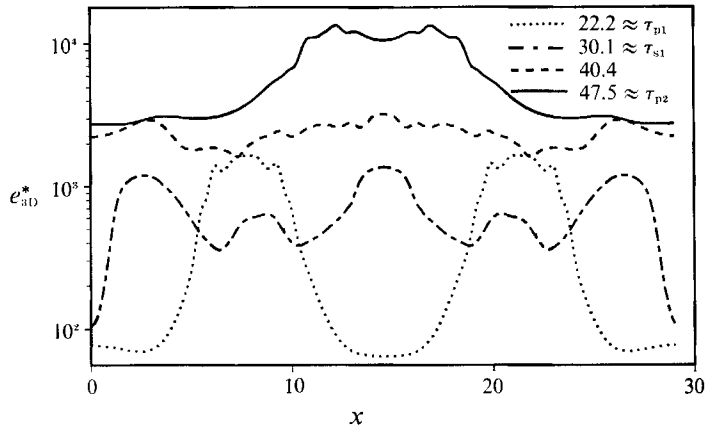

FIGURE 7. Normalized perturbation energy density e^*_{3D} as a function of x at the four times indicated in the legend for a $\beta = 1$ perturbation evolving on a base flow undergoing two pairings (2D2P)

precise measure of when new perturbation spanwise vorticity (required for circulation growth) crosses the mid-braid plane (MP). Spanwise vorticity that is weaker than that still present in the MP re-enters before τ_{00}. This effect is accentuated in this case because the competition between pairing and oversaturation causes the spanwise vorticity to approach and cross the MP very slowly. This is also the reason the circulation grows gradually instead of jumping as in the other re-entries.

The evolution of A^*_{3D} can be further studied by examining the three-dimensional disturbance energy density given by

$$e_{3D} = \frac{1}{L_z}\int_{-\infty}^{\infty}\int_0^{L_z} u_i u_i - \langle u_i\rangle_z \langle u_i\rangle_z \,\mathrm{d}z\,\mathrm{d}y, \tag{12}$$

where $\langle\ \rangle_z$ is the spanwise average. The amplitude A^*_{3D} is related to the normalized energy density ($e^*_{3D} = e_{3D}/e^0_{3D}$)† by

$$A^*_{3D} = \left[\frac{1}{L_x}\int_0^{L_x} e^*_{3D}\,\mathrm{d}x\right]^{\frac{1}{2}}. \tag{13}$$

In figure 7, e^*_{3D} is shown as a function of x for the two-pairing case 2D2P at several times between the first and second pairings. At τ_{p1}, the energy is concentrated in the cores of the rollers. (At τ_{p1}, the paired rollers are centred at $x = 7.8$ and 21.4. At τ_{p2} the single remaining roller is centred at $x = 14.6$.) As the spiral arms enter the braid regions (see §3), energy is transferred out of the core and into the braid regions, causing the energy in the braid regions to grow. By τ_{s1}, the maximum braid region energy density is a factor of two greater than that in the cores. Also, note that at this time the MP of the braid region to be engulfed in the next pairing ($x = 14.6$) has experienced a large growth while the surviving MP ($x = 0$ and $x = 4\lambda_x = 29.2$) has not. This is because at τ_{s1} the spiral arms have just crossed the surviving MP and energy growth is just starting. The fact that the spiral arms enter parts of the braid region and initiate circulation and energy growth before they ultimately reach the surviving MP is the reason that A^*_{3D} leaves its plateau and begins growing well before τ_{s1}. Later ($t = 40.4$), the energy continues to grow at all x such that it becomes roughly uniformly distributed. Finally, at the second pairing, the energy has again

† Note that because the initial three-dimensional disturbance is streamwise invariant, e^0_{3D} is independent of x.

grown larger in the core than in the braid region. Note that the energy is more highly concentrated in the cores at the first pairing than at the second. This is because of the greater complexity of the perturbations at the second pairing (see §4.2). Between $t = 40.4$ and $t = \tau_{p2}$, the energy density is growing only in the roller core, since the spanwise vorticity has again been removed from the braid region. Finally, by τ_{p2}, A^*_{3D} stops growing for a while (during the plateau regions in figure 5). At this point e^*_{3D} in the surviving MP is constant and the only changes occurring in the e^*_{3D} profile consist of mild redistributions of energy in the roller core. Apparently the roller disturbances come into some sort of temporary 'equilibrium' with the braid disturbances, which can no longer grow. The above process is repeated as another spiral-arm re-entry and pairing occur.

Another consequence of the growth scenario discussed above is that the long-term growth of the three-dimensional perturbations in the presence of pairings is algebraic rather than exponential. One way to see this is to consider the circulation evolution. The above discussion suggests that the magnitude of the circulation jump that occurs at each spiral-arm re-entry should be proportional to the circulation just before the jump because the circulation jump is governed by the spanwise vorticity disturbance brought into the mid-braid plane. The strength of this vorticity disturbance should be proportional to the circulation level since the roller and ribs have 'equilibrated'. There may also be a weak dependence on the pairing number or other details of the two-dimensional flow. This is supported by the results in figure 5 where the circulation appears to jump by a constant factor at each τ_{sn}. Thus $\Gamma^*_x \sim \Gamma_j^{N_p}$, where N_p is the pairing number and $\Gamma_j \approx 6$ is the factor by which the circulation jumps at each τ_{sn}. On the other hand, the time between jumps should scale approximately as 2^{N_p}, since the length- and timescales roughly double at each pairing (§3). Therefore $\Gamma^*_x \sim A^*_{3D} \sim t^{\log_2 \Gamma_j}$. A similar conclusion is reached if one assumes that, since the length- and timescales are growing like t, the average growth rate (σ) of the perturbations varies like $\sigma \sim 1/t$. On the other hand, the length- and timescales would no longer grow linearly if pairing were suppressed. In this case, spanwise vorticity from the oversaturated roller continually occupies the braid region, resulting in continuous circulation growth. The growth is then apparently exponential, in agreement with the results of Pierrehumbert & Widnall (1982), whose model problem (the Stuart 1967 vortices) is similar to an array of oversaturated rollers. Since the long-term growth of the three-dimensional perturbations in the presence of pairings is algebraic, the degree of three-dimensionality one ultimately obtains in any finite time depends greatly on the magnitude of the initial (or inlet) disturbances.

4.2. *Structure of the linear perturbations*

The structure of the three-dimensional perturbations is of interest since, as noted in RM, similar features are present in fully nonlinear simulations well past the onset of three-dimensional nonlinearity. The streamwise vorticity of the $\beta = 1$ perturbations at the first three pairing times and the associated spiral-arm re-entry times is shown in figure 8. At each time, the streamwise vorticity associated with the ribs is clearly visible. However, as spanwise vorticity in the spiral arms is brought into the braid region, streamwise vorticity perturbations are present far from the centre of the layer in the braid region (figure 9*b*). They are then brought together by the two-dimensional strain in the braid region, as shown in figure 9. In the MP, the pattern of streamwise vorticity resembles five pairs of ribs stacked on top of each other. These distinct regions of streamwise vorticity are eventually pressed together by the strain, allowing viscosity to merge them so that only one region is apparent by

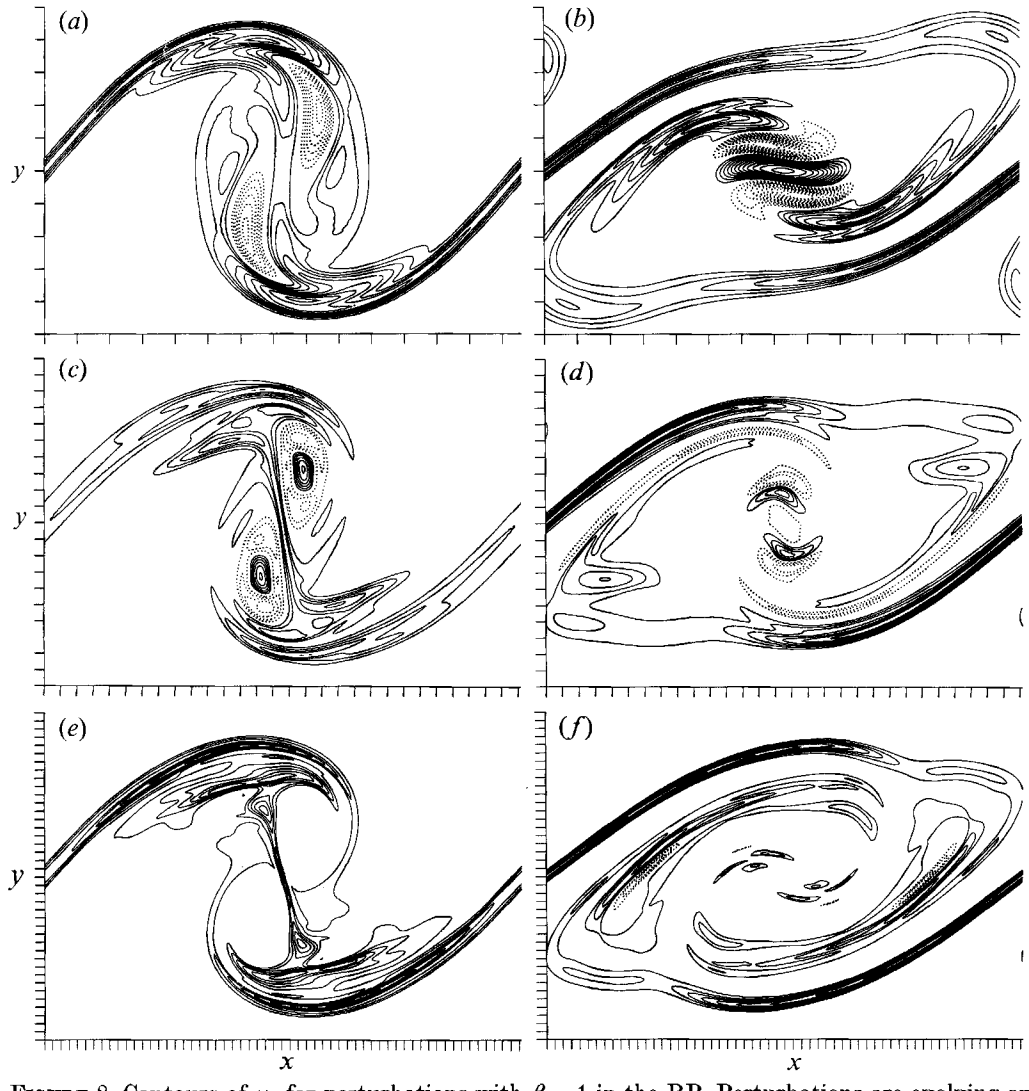

FIGURE 8. Contours of ω_x for perturbations with $\beta = 1$ in the RP. Perturbations are evolving on a base flow undergoing (*a*, *b*) one, (*c*, *d*) two and (*e*, *f*) three pairings (2D1P, 2D2P, and 2D3P respectively). Times are (*a*) $21.5 = \tau_{p1}$, (*b*) $30.4 \approx \tau_{s1}$, (*c*) $47.5 \approx \tau_{p2}$, (*d*) $63.8 \approx \tau_{s2}$, (*e*) $104.8 \approx \tau_{p3}$, and (*f*) $140.1 \approx \tau_{s3}$. The contour increments are (*a*, *b*) $1.5\Gamma_x^0/(\delta_\omega^0)^2$, (*c*, *d*) $5\Gamma_x^0/(\delta_\omega^0)^2$, and (*e*, *f*) $16\Gamma_x^0/(\delta_\omega^0)^2$.

the next pairing (figure 8*c*). This amalgamation of streamwise vorticity occurs by a different mechanism for finite-amplitude disturbances (see RM and §5). Similar layered vorticity patterns form in the braid regions after further pairings (figure 8*d*, *f*).

Also apparent in these figures is the streamwise vorticity in the roller cores. At the first pairing (τ_{p1}), the streamwise vorticity associated with each of the original unpaired rollers is visible as a large region of negative vorticity. For each pairing, the relative magnitude of the streamwise vorticity disturbances remaining in the prepairing cores is smaller until, at τ_{p3} (figure 8*e*), there is virtually no streamwise vorticity disturbance left in the cores. The other vorticity components are also small

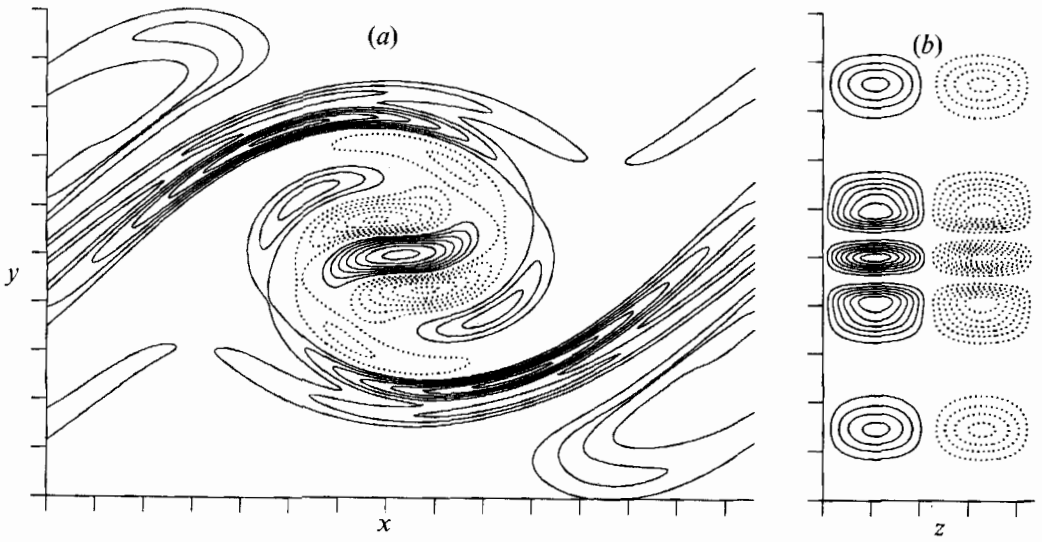

FIGURE 9. Contours of ω_x in the (*a*) RP and (*b*) MP for a perturbation with $\beta = 1$ evolving on a single-pairing base flow (2D1P); $t = 35.1$ (a time after that in figure 8*b*). The contour increments are (*a*) $3\Gamma_x^0/(\delta_\omega^0)^2$ and (*b*) $\Gamma_x^0/(\delta_\omega^0)^2$.

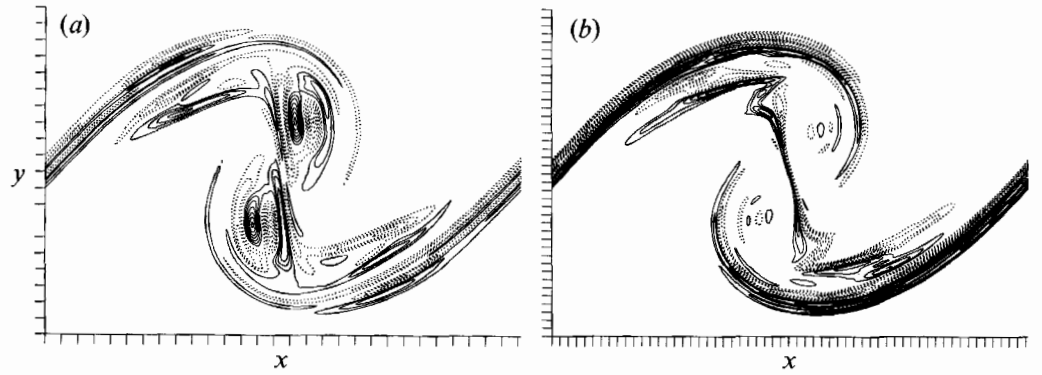

FIGURE 10. Contours of perturbation spanwise vorticity (ω_z^{3D}) in the RP of $\beta = 1$ perturbations evolving on a (*a*) two-pairing (2D2P) and (*b*) three-pairing (2D3P) base flow. Times are (*a*) $47.5 \approx \tau_{p2}$ and (*b*) $104.8 \approx \tau_{p3}$. The contour increment is $12\Gamma_x^0/(\delta_\omega^0)^2$.

in the prepairing cores at τ_{p3}. At the same time, the streamwise vorticity disturbances away from the core become more complicated, with finer structure relative to the size of the roller. This is expected since the effective Reynolds number is doubling with each pairing. Also, with each additional pairing, the disturbance is 'folded over' (like kneading bread) resulting in more striated disturbances. This is especially apparent in the perturbation spanwise vorticity disturbances ($\omega_z^{3D} = \omega_z - \langle\omega_z\rangle_z$) shown at the second and third pairings in figure 10. It is important to recall that these very complicated perturbation flows are a result of a linear evolution. The source of the complexity is the evolving base flow, not three-dimensional nonlinearity. Even with these differences between the disturbances at different pairings (disturbance levels in the cores, and fineness of striations), several of the qualitative features of the vorticity fields are the same during the second and third pairings (see figures 8 and 10).

Simulation	A_{10} $\times 10^2$	$A_{\frac{1}{2}0}$ $\times 10^2$	$A_{\frac{1}{4}0}$ $\times 10^2$	A_{01}† $\times 10^2$	$A_{0\frac{1}{2}}$† $\times 10^2$	$A_{0\frac{1}{4}}$† $\times 10^2$	$\phi_{0\frac{1}{2}}$	$\phi_{0\frac{1}{4}}$	τ_r	τ_{o0}	τ_{p1}	τ_{s1}	τ_{p2}	τ_{s2}
HIGH0P	4.00	—	—	8.32	—	—	—	—	12.4	15.9	—	—	—	—
LOW1P	4.00	3.00	—	1.66	—	—	—	—	11.9	—	21.6	28.8	—	—
HIGH1P	4.00	3.00	—	8.32	—	—	—	—	11.5	—	23.4	27.4	—	—
LOW2P	$4.52^{\omega G}$	$3.47^{\omega G}$	$5.14^{\omega G}$	1.59	—	—	—	—	11.8	—	21.1	32	40.0	53
MID2P	$4.52^{\omega G}$	$3.47^{\omega G}$	$5.14^{\omega G}$	3.18	—	—	—	—	11.8	—	21.1	32	40.3	54
HIGH2P	$4.52^{\omega G}$	$3.47^{\omega G}$	$5.14^{\omega G}$	9.64^{vG}	—	—	—	—	11.2	—	20.1	31.2	38.3	T
WMID2P	$4.52^{\omega G}$	$3.47^{\omega G}$	$5.14^{\omega G}$	3.18	1.02	1.54	0	0	11.8	—	21.1	31	40.1	54
WHIGH2P	$4.52^{\omega G}$	$3.47^{\omega G}$	$5.14^{\omega G}$	9.64^{vG}	2.71^{vG}	1.54	0	0	11.2	—	20.4	31	38.5	T
TURB2P	4.00	3.00	3.00	8.32	6.66	10.11	$\frac{1}{8}\pi$	$\frac{7}{16}\pi$	11.3	—	21.0	29.2	47.1	T

† For comparison with cases cited in RM, $\Gamma_x/A_{0\beta} = 4.382$, 5.472 and 7.210 for ω-Gaussian disturbances with $\beta = 1$, $\frac{1}{2}$ and $\frac{1}{4}$ respectively. For v-Gaussian disturbances $\Gamma_x/A_{0\beta} = 4(\frac{1}{2}\pi)^{\frac{1}{4}} k_z/(k_z^2+1)^{\frac{1}{2}}$, where $k_z = 2\pi\beta/\lambda_z$.

TABLE 2. Parameters of the three-dimensional simulations. Two-dimensional disturbance profiles are eigenfunctions unless superscripted $^{\omega G}$, in which case they are ω-Gaussian. Three-dimensional disturbance profiles are ω-Gaussian unless superscripted ^{vG}, in which case they are v-Gaussian. $Re_0 = 250$, $\phi_{\alpha 0} = 0$, $\lambda_x = 1.16\,(2\pi)$, $\lambda_z = 0.6\lambda_x$ and $Pr = 1.0$ for all cases. A 'T' indicates that the flow is too 'turbulent' for τ_{s2} to be well-defined. Numbers given with less precision (τ_{sn}) are the result of $-\omega_b$ not being computed at every time step for some simulations. All the flows were either too 'turbulent' or not computed long enough to determine τ_{o1} and τ_{o2}. The HIGH0P simulation was referred to as LOWDEL in Rogers & Moser (1991).

5. Three-dimensional pairings

In this section the nonlinear evolution of a mixing layer undergoing one pairing is examined. Results from two simulations with different initial three-dimensional disturbance strengths are studied and compared with the linear analysis discussed in §§4.1 and 4.2. Table 2 lists some characteristics of the initial conditions for these two simulations (LOW1P and HIGH1P) along with values of several of the reference times defined and used in this paper; other simulations referred to later in the paper are included in the table as well. In both simulations, the initial three-dimensional perturbation is in the fundamental (0, 1) Fourier mode (see (9)).

5.1. *Weakly three-dimensional pairing*

In RM it was found that the evolution of infinitesimal three-dimensional perturbations provided a good approximation of finite-amplitude perturbations even after the onset of three-dimensional nonlinearity. This is also true for flows undergoing pairings. In figure 11, the evolution of the normalized three-dimensional amplitude A_{3D}^* and the normalized circulation Γ_x^* for both the LOW1P and HIGH1P flows are compared to the results of the linear analysis of §4. These three simulations were begun from initial conditions that are identical except for the strength of the three-dimensional perturbation, with LOW1P having a three-dimensional perturbation a factor of 5 weaker than HIGH1P (see table 2). As can be seen in figure 11, both the amplitude and circulation of LOW1P evolve nearly as predicted by linear analysis, with some slight differences occurring during and after the pairing. In contrast, the stronger perturbation in HIGH1P results in some departure from the linear evolution as soon as $t = 5$.

Despite the good agreement between linear analysis and the LOW1P simulation, there are some nonlinear effects at, and beyond, the first pairing. For example, by τ_{s1} the ribs in LOW1P begin a marginal collapse in agreement with the Lin & Corcos

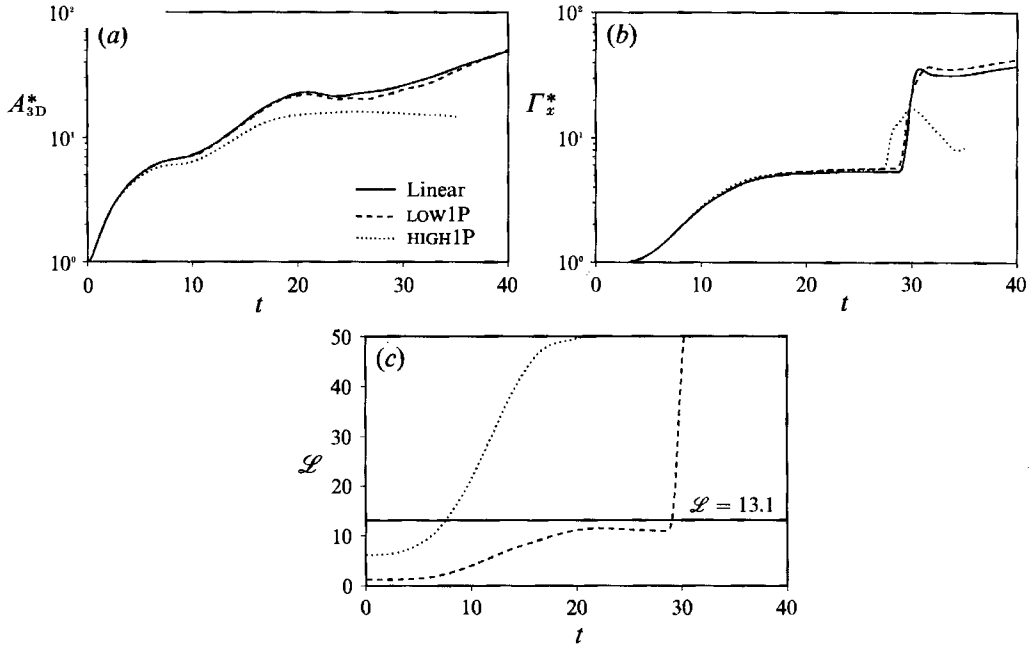

FIGURE 11. Time development of (*a*) A^*_{3D}, (*b*) Γ^*_x, and (*c*) the Lin & Corcos (1984) collapse parameter $\mathscr{L}$ for various levels of initial three-dimensionality. Note $\mathscr{L} = 0$ for linear analysis.

collapse criterion (see figure 11*c* and RM, $\mathscr{L}$ defined in (A 3)). Otherwise, the streamwise vorticity in LOW1P (see Moser & Rogers 1992) is virtually identical to the corresponding linear perturbation shown in figure 8. Note that the same level of three-dimensionality in non-pairing flows resulted in no discernible differences until after τ_{00} (see RM).

In contrast, at τ_{p1} there are significant differences in the perturbation spanwise vorticity (ω_z^{3D}) in the BP of LOW1P, due to nonlinear evolution of the 'cups' (discussed in RM), which are visible in figure 12(*b*) as the two intense regions of negative perturbation. Also note that the linear perturbations have the following symmetry:

$$\left.\begin{aligned} \omega_i(x,y,z) &= \omega_i(-x+2x_s,-y,z), \quad i=x \quad \text{or} \quad y, \\ \omega_z^{3D}(x,y,z) &= -\omega_z^{3D}(-x+2x_s,-y,z), \end{aligned}\right\} \tag{14}$$

where $x_s = 0$ or $\frac{1}{2}\lambda_x$. This symmetry is preserved by the linearized equations but not by the Navier–Stokes equations. Thus the symmetry is not apparent in figure 12(*b*). As the flow evolves further, the structural differences between LOW1P and the corresponding linearly evolving flow increase. The magnitude of the linear spanwise vorticity perturbation continues to grow while that of LOW1P does not (see figure 12). By $t = 40$, there is little similarity between ω_z^{3D} of LOW1P and the linear analysis. Especially apparent is the absence of perturbations in the braid regions of LOW1P (figure 12*d*). The differences in the magnitude of ω_z^{3D} can be quantified by examining the spanwise vorticity amplitude, W_{z3D} (defined analogously to the amplitude A_{3D}, with the spanwise vorticity replacing the velocity in (6) and (7)), normalized by $\Gamma^0_x/\delta^{02.5}_\omega$. The normalized W_{z3D} is 48% lower in LOW1P at τ_{s1} (5.80 and 8.57 for the LOW1P and linear cases respectively), and is more than a factor of two smaller in LOW1P at $t = 40$ (6.36 versus 14.65). Despite this large difference in W_{z3D}, the discrepancies in the magnitudes of the other vorticity components and the velocity

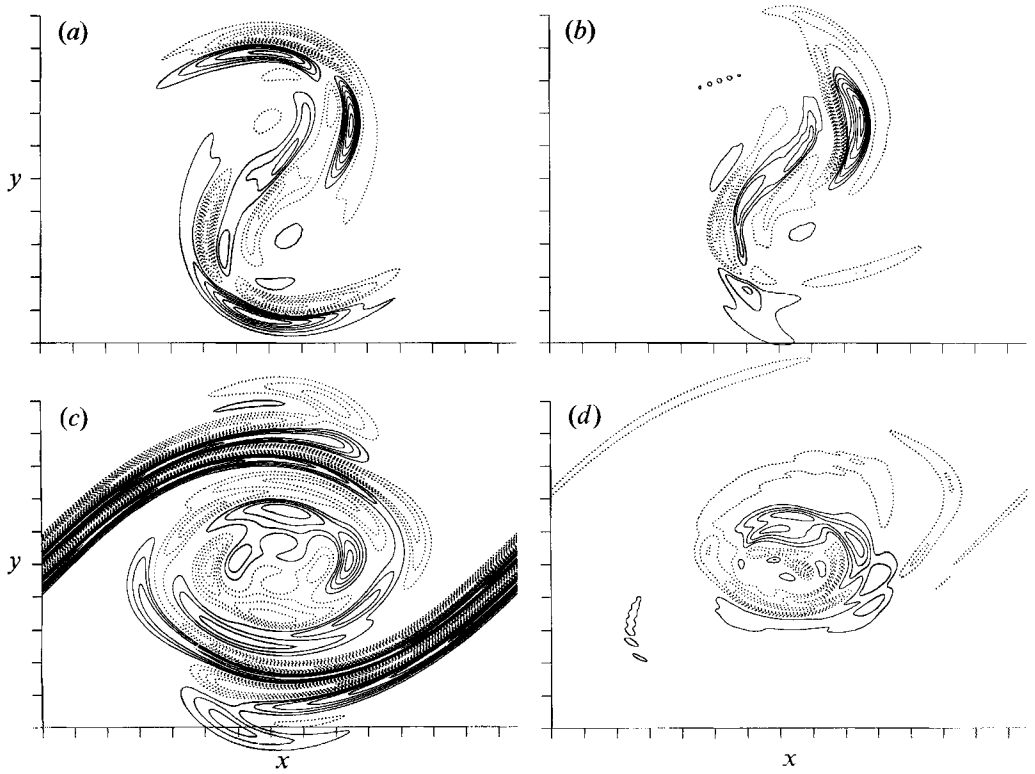

FIGURE 12. Contours of perturbation spanwise vorticity (ω_z^{3D}) in the BP at (a, b) $t = 22.6 \approx \tau_{p1}$ and (c, d) $t = 40.0$ for (b, d) LOW1P and (a, c) the corresponding linear analysis (base flow 2D1P). Contour level is $3\Gamma_x^0/(\delta_\omega^0)^2$. In this and subsequent similar figures, dotted contours indicate negative vorticity, solid contours positive vorticity, and tick marks are at δ_ω^0 increments.

components are less than 8% at $t = 40$. It is remarkable that such large three-dimensional nonlinearities occur in the perturbation spanwise vorticity, with little or no effect on other quantities.

5.2. *Highly three-dimensional pairing*

The HIGH1P flow described in this section results from an initial streamwise-invariant disturbance of the same amplitude as that used in the ROLLUP case described in RM (a factor of 5 larger than in LOW1P). As expected, the early evolution of HIGH1P is very similar to that of its non-pairing counterpart. In particular, the prepairing evolution of HIGH1P is characterized by the same 'cups' and collapsed 'ribs' that were described in detail in RM (see Moser & Rogers 1992). A quantitative comparison between the evolution of mid-braid spanwise vorticity, mid-braid strain rate, momentum thickness, and Lin & Corcos (1984) collapse parameter in HIGH1P, HIGH0P (corresponding non-pairing flow), and the corresponding two-dimensional flow (2D1P) is given in figure 13. The differences between HIGH1P and HIGH0P become significant by $\tau_{\omega 0} = 15.9$ of HIGH0P as expected, since oversaturation does not occur in HIGH1P at this time.

As with the non-pairing flows discussed in RM, HIGH1P is highly three-dimensional and undergoes significant three-dimensional nonlinear evolution (see figure 11). In fact, the three-dimensional amplitude (A_{3D}) exceeds the two-dimensional amplitude (A_{s0}) for most of the evolution (figure 14). The three-dimensionality also affects the

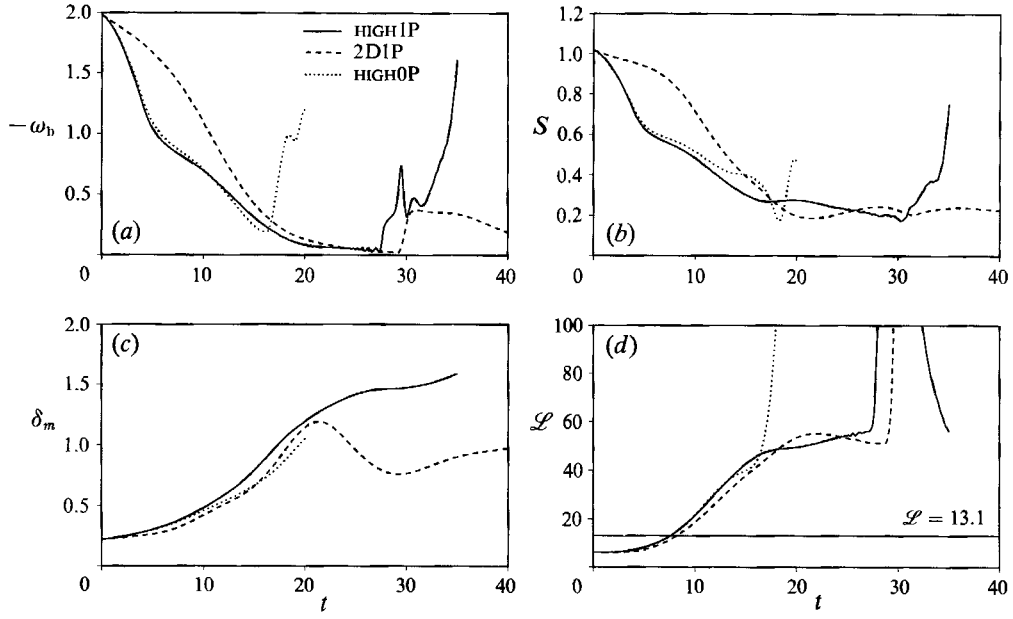

FIGURE 13. Time development of (*a*) mid-braid vorticity, (*b*) mid-braid strain rate, (*c*) momentum thickness, and (*d*) the Lin & Corcos (1984) collapse parameter. In (*d*), the curve labelled 2D1P was obtained by scaling Γ_x^0 of the infinitesimal perturbation to be the same as the value in HIGH1P.

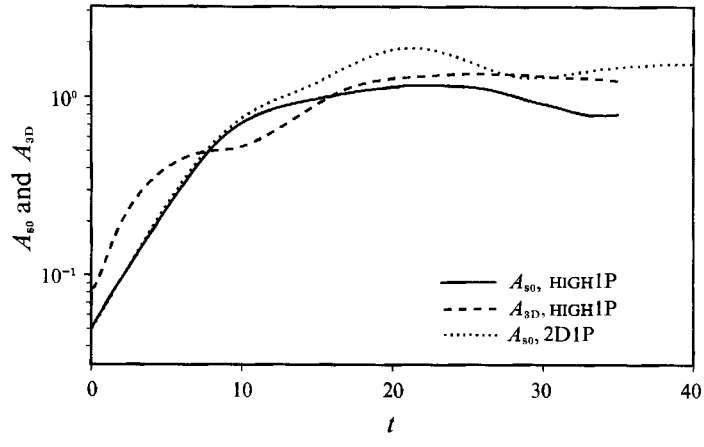

FIGURE 14. Time development of disturbance amplitudes for HIGH1P and the corresponding two-dimensional case (2D1P).

two-dimensional modes as evidenced by the differences in A_{s0} and the pairing times τ_{p1} between HIGH1P and 2D1P (see tables 1 and 2 and figure 14). Despite the strong three-dimensionality of this flow, the circulation of the rib vortices (Γ_x) is well predicted by the linear computations until τ_{s1} (see figure 11*b*), as are the plateau levels of mid-braid vorticity and strain rate ($-\omega_b$ and S, see figure 13). Thus, the plateau level of the Lin & Corcos (1984) collapse parameter can be well predicted in this flow by scaling the linear results (figure 13*d*).

As was discussed in Moser & Rogers (1991), pairing in this flow ultimately results in a transition to turbulence. This process is depicted in more detail for HIGH1P in figures 15 and 16, where the spanwise vorticity in the between-ribs plane (BP) and

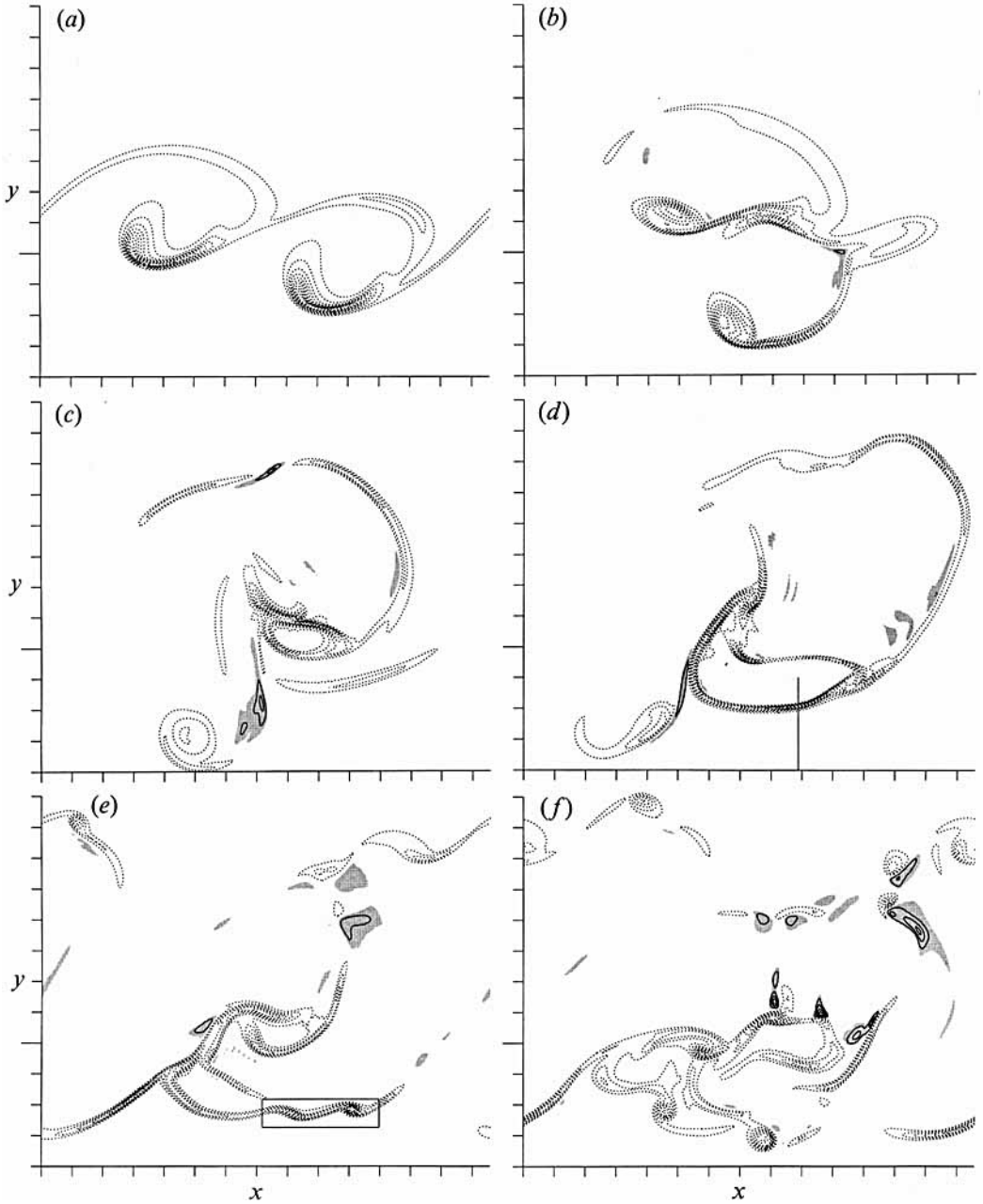

FIGURE 15. Contours of ω_z in the $z = 0$ BP of HIGH1P at (*a*) $t = 14.6$, (*b*) $t = 19.3$, (*c*) $t = 23.5 \approx \tau_{p1}$, (*d*) $t = 27.3 \approx \tau_{s1}$, (*e*) $t = 29.8$ and (*f*) $t = 35.0$. The contour increments are (*a*, *b*, *f*) ± 0.6 and (*c*, *d*, *e*) 0.8 ($1.65\Gamma_x^0/(\delta_\omega^0)^2$ and $2.20\Gamma_x^0/(\delta_\omega^0)^2$ respectively). Regions of positive spanwise vorticity are shaded. $y = 0$ is at the long tick-mark, not the centre of the domain. The secondary rollup marked with a box in (*e*) and the plane given by the vertical line in (*d*) are discussed in §5.2.2.

rib plane (RP) is shown. There are several key features of this development that were noted in Moser & Rogers (1991). The cups of intense spanwise vorticity discussed in RM are visible in figure 15(*a*). They begin to interact (figure 15*b*) and are torn apart (figure 15*c*). The spanwise vorticity in the BP then reorganizes into thin sheets

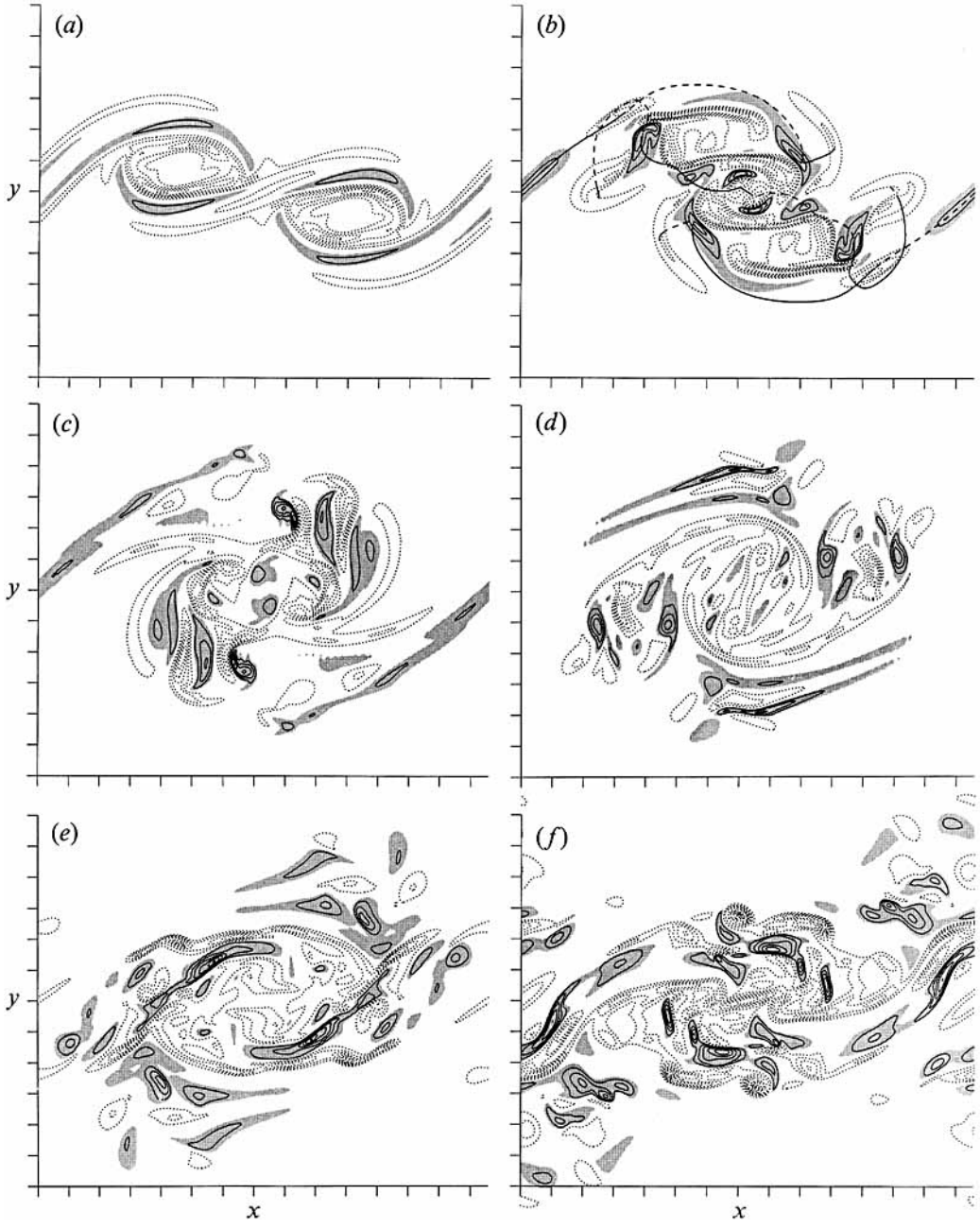

FIGURE 16. Contours of ω_z in the $z = \frac{1}{4}\lambda_z$ RP of HIGH1P at (*a*) $t = 14.6$, (*b*) $t = 19.3$, (*c*) $t = 23.5 \approx \tau_{p1}$, (*d*) $t = 27.3 \approx \tau_{s1}$, (*e*) $t = 29.8$ and (*f*) $t = 35.0$. The contour increments are (*a*, *b*, *f*) ± 0.6 and (*c*, *d*, *e*) ± 0.8 ($1.65\Gamma_x^0/(\delta_\omega^0)^2$ and $2.20\Gamma_x^0/(\delta_\omega^0)^2$ respectively). Regions of positive spanwise vorticity are shaded. In (*b*) the heavy dark lines are rib vortex lines; they are dashed when the vortex line is behind the RP.

(figure 15*d*) that subsequently undergo secondary rollups (figure 15*e*). During the same time, the relatively simple prepairing spanwise vorticity pattern in the RP (figure 16*a*, *b*) is transformed into an apparently turbulent vorticity distribution (figure 16*f*), with many small-scale granular regions of both signs of spanwise

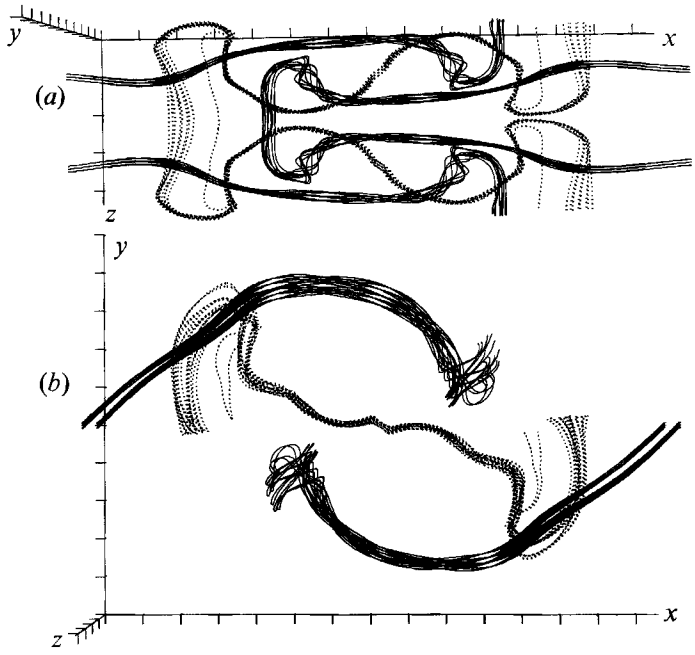

FIGURE 17. Vortex lines that pass through or near the symmetry points in the surviving (solid) and engulfed (dotted) ribs for HIGH1P at $t = 19.3$; (*a*) top view and (*b*) side view.

vorticity. The flow rapidly becomes too complex to allow a detailed description of the development of all its features, but the analysis presented below does yield some insight into the processes underlying this transition.

As in RM, the two symmetries (10) and (11), which are both present in HIGH1P, simplify the analysis of the flow. Because of the point symmetry (11), the rib vortices are constrained to be centred at the symmetry points and the vortex lines associated with the ribs can be unambiguously defined. In HIGH1P there are symmetry points in both the surviving and engulfed braid regions, so both sets of rib vortex lines can be tracked. The plane symmetry (10) requires that w, ω_x, and ω_y be zero in the between-ribs plane (BP). Therefore, the equation governing the spanwise vorticity in the BP is particularly simple:

$$\frac{\partial \omega_z}{\partial t} + u\frac{\partial \omega_z}{\partial x} + v\frac{\partial \omega_z}{\partial y} = \omega_z \frac{\partial w}{\partial z} + \frac{1}{Re}\left(\frac{\partial^2 \omega_z}{\partial x^2} + \frac{\partial^2 \omega_z}{\partial y^2}\right) + \frac{1}{Re}\frac{\partial^2 \omega_z}{\partial z^2}. \tag{15}$$

This is the two-dimensional vorticity equation except for the single stretching term $(\omega_z \partial w/\partial z)$ and the spanwise diffusion term $(1/Re)\,\partial^2 \omega_z/\partial z^2)$.

5.2.1. *Evolution of rib vortex lines*

In RM it was shown that the rib vortex lines leave the RP and are twisted around each other near a horseshoe tip that connects one rib vortex with its neighbour. This distortion gives rise to the positive spanwise vorticity regions in the rib plane as in figure 16(*a*). Such distortion of rib vortex lines was seen to be the major source of positive spanwise vorticity in the absence of pairings (RM). Rib vortex lines at $t = 19.3$ are shown in figure 17. The vortex lines for both the surviving ribs and the engulfed ribs are highly distorted, with large excursions out of the rib plane. Note that at several points, the vortex lines through neighbouring engulfed ribs are

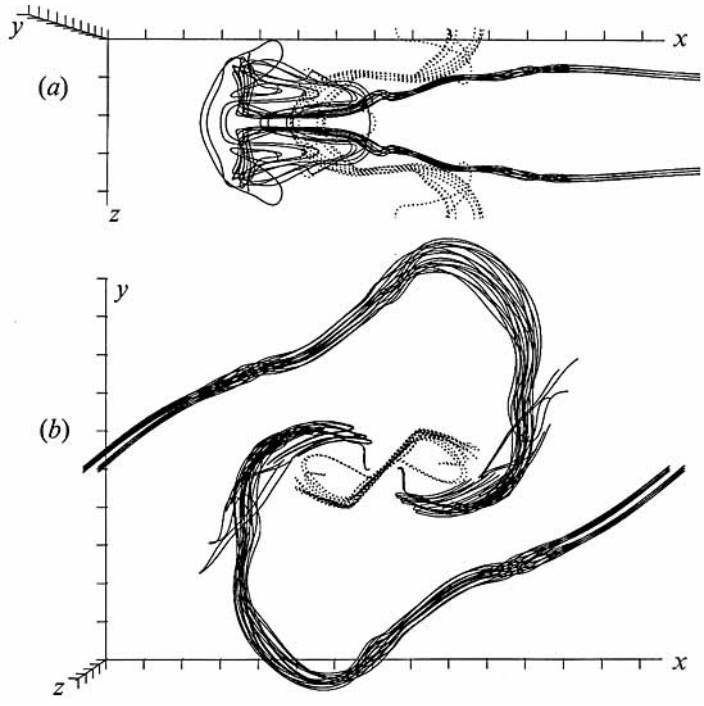

FIGURE 18. Vortex lines that pass through or near the symmetry points in the surviving (solid) and engulfed (dotted) ribs for HIGH1P at $t = 23.5 \approx \tau_{p1}$: (*a*) top view and (*b*) side view. Only one set (right side) of surviving ribs are included in (*a*).

coming very close together. This proximity allows viscosity to reconnect the vortex lines, yielding a different topology at a later time. This has already begun to occur, as is evidenced by the small regions of positive spanwise vorticity in the BP at this time (figure 15*b*). Initially, the spanwise vorticity is all negative in this plane. According to (15), the only way positive spanwise vorticity can arise in the BP is by viscous diffusion in the spanwise direction. At several locations this diffusion results in viscous reconnection of the vortex lines. The positive regions of spanwise vorticity in figure 15(*b*) are located where the engulfed rib vortex lines in figure 17 are pinched together. It is interesting to note that in this very complicated flow, the topology of the vortex lines associated with the major structures is still largely that of the initial vortex sheet, i.e. there has been almost no vortex reconnection to form closed vortex loops or vortex lines running counter to the mean vorticity across the entire spanwise domain.

Where the rib vortex lines cross the rib plane, there must be a region of non-zero spanwise vorticity. The correspondence of features in the spanwise vorticity contours with rib vortex line crossings is shown in figure 16(*b*). Note that almost all the regions of non-zero spanwise vorticity are associated with the crossing of rib vortex lines. The major exceptions are the four long thin regions of particularly strong vorticity associated with the cup structures. There are also two small positive regions near the centre of the roller that are associated with the 'sub-rib' structures discussed in RM. The spanwise vorticity pattern in the between plane can also be understood in terms of the cups and wisps associated with the rib and sub-rib vortex lines (see RM). Thus, the features of the mixing layer at this time are manifestations of the structures present in the non-paired layer.

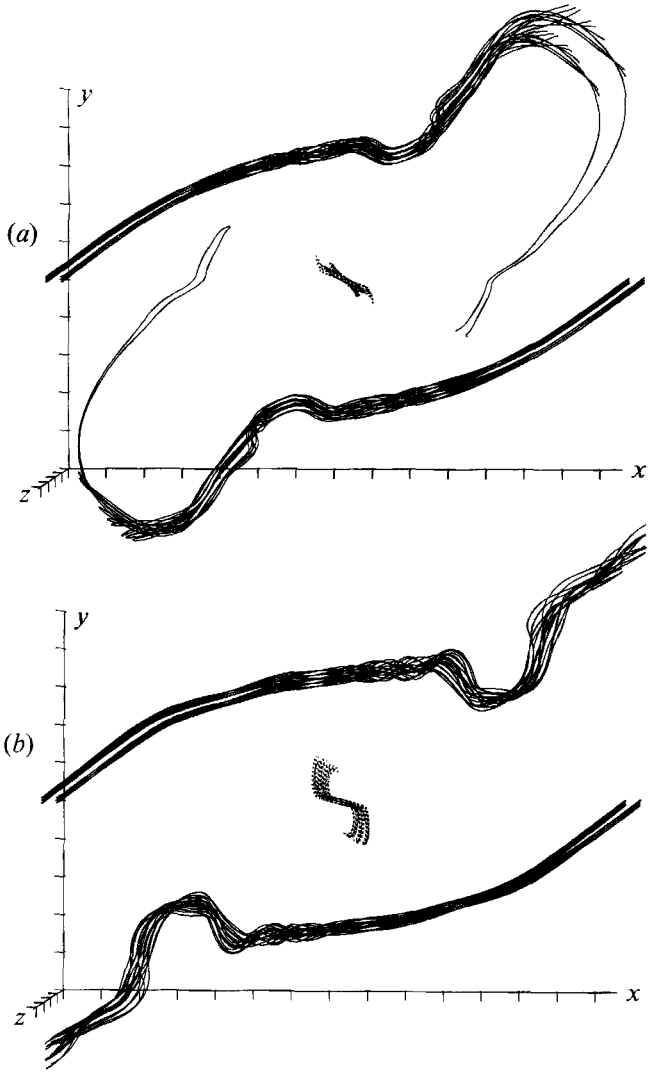

FIGURE 19. Vortex lines that pass through or near the symmetry points in the surviving (solid) and engulfed (dotted) ribs for HIGH1P at (*a*) $t = 27.3 \approx \tau_{s1}$ and (*b*) $t = 31.1$.

The correspondence of vorticity structures to the prepairing ribs and cups does not persist for long. By $t = 23.5 \approx \tau_{p1}$ the vorticity in the roller can no longer be described in terms of these original structures. Vortex lines through (and near) the engulfed-rib symmetry point in the middle of the paired roller (figure 18) no longer have the large excursions shown in figure 17, indicating that the topology of the vorticity has changed as a result of viscous reconnection. Thus, at this time, the vortex lines passing through the engulfed-rib symmetry point can no longer be identified as an engulfed rib. The cup structures are also not identifiable at this time, so the only persisting major features of the prepairing mixing layer are the surviving ribs. Vortex lines representing the surviving ribs at $t = 23.5 \approx \tau_{p1}$, $t = 27.3 \approx \tau_{s1}$ and $t = 31.1$ are shown in figures 18 and 19. At τ_{p1}, the main rib vortex lines are wrapped into the pairing roller, although they extend far above and below the roller before doing so. At the point of greatest excursion (in y), lines from neighbouring ribs are

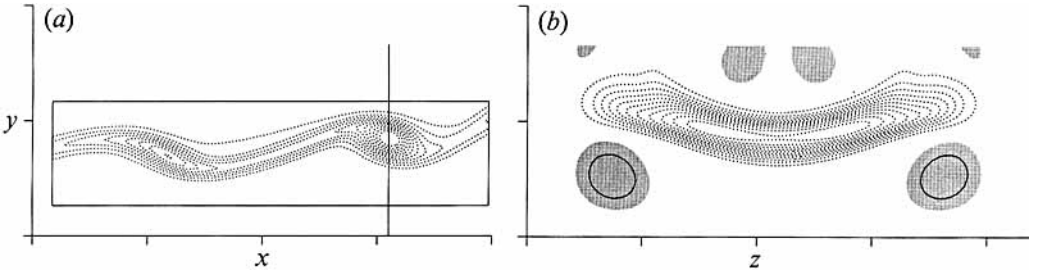

FIGURE 20. (*a*) Enlargement of the ω_z contours in the boxed region of figure 15(*e*). (*b*) ω_z contours in the (z, y)-plane passing through the centre of the right roller in (*a*). The contour increment is ± 0.8. Regions of positive ω_z are shaded. The domain is $7 \leqslant x \leqslant 11$, $-3 \leqslant y \leqslant -1$ and $0 \leqslant z \leqslant \lambda_z$.

being pinched together, allowing viscosity to reconnect them. This has been largely completed by τ_{s1} (figure 19*a*). At this time the rib vortex lines again connect to the neighbouring ribs far from the rollers, this time through the wisp of spanwise vorticity shown in figure 15(*d*).

It is this wisp of spanwise vorticity that crosses the MP at τ_{s1}, leading to the circulation jump at that time. Thus, as in RM, the circulation jump at τ_{s1} occurs because the rib vortices are pulled over (or under) the roller into the neighbouring braid region. When the vortex lines are pulled all the way through the MP (at about $t = 30$; figure 19*b* is just after this), the circulation should have tripled, since then vortex lines from three sets of ribs cross the MP (the original rib and the ribs from braid regions up- and downstream). The actual maximum circulation jump (from 2.05 before τ_{s1} to 6.33 at $t = 30$, see figure 11*b*) is slightly more than a factor of three.

At $t = 30$, the mid-braid circulation of HIGH1P (figure 11*b*) reaches a maximum and begins a rapid decline. This is also caused by spanwise vorticity entering the braid region, but in this case the vortex lines associated with it are kinked in a sense opposite to that of the rib lines. The spanwise vorticity structure that causes the circulation decline is apparent in figure 15(*e*) (the long thin sheet of spanwise vorticity in the lower left portion of the domain). It is not surprising that these vortex lines are kinked in the opposite sense to the ribs since most of the prepairing core vortex lines are kinked in this way.

5.2.2. *Formation and evolution of vortex sheets*

The thin sheets of spanwise vorticity that form in the BP become very long and wide compared to their thickness. For example, the boxed region in figure 15(*e*) has been magnified in figure 20(*a*), along with a z, y cross-section through the right roller in that region. Since this is essentially a two-dimensional vortex sheet, it is no surprise that it is undergoing a Kelvin–Helmholtz rollup, as noted in Moser & Rogers (1991). The velocity profile averaged in x over the extent of the box in figure 20(*a*) is shown in figure 21. The average velocity jump across this mini-mixing layer is approximately 0.8 and the vorticity thickness is approximately 0.27. (The unaveraged velocity jump across the internal shear layer is as high as 1.3 at the right rollup in figure 20*a*.) The most unstable wavelength of such a shear layer is about 2.0, which is in good agreement with the spacing between the forming rollers in figure 20(*a*). This secondary rollup of the internal shear layer continues until, by $t = 35$, individual rollers have developed (the two rollers in the bottom of the domain of figure 15*f*). At this time there are also other internal shear layers that are beginning to roll up (see figure 15*f*). The formation of thin internal shear layers in the BP and

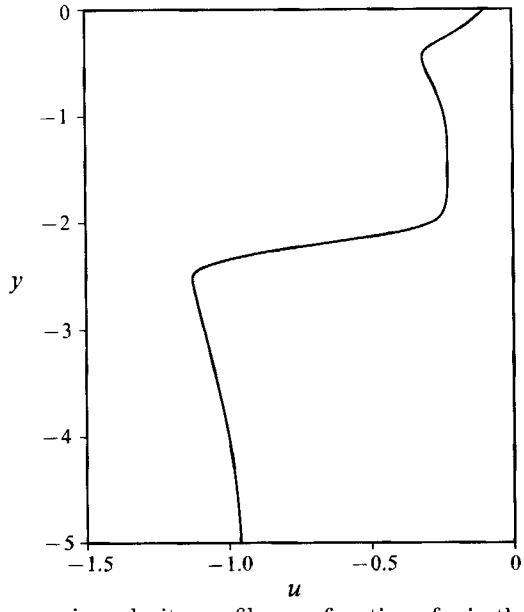

FIGURE 21. Streamwise velocity profile as a function of y in the BP, averaged over the x-domain defined by the box in figures 15(*e*) and 20(*a*).

their subsequent rollup increases the complexity of the flow and contributes to the cascade to small scales and the development of turbulence.

According to (15), the only way that spanwise vorticity can be amplified in the BP is by stretching in the z-direction. This must therefore be responsible for the formation of the thin sheets of spanwise vorticity discussed above. In the case of the thin sheet that is shown rolling up in the box in figure 15(*e*), this strain is primarily due to the surviving rib vortices. At $t = 27.3 \approx \tau_{s1}$, when the vortex sheet is forming (see figure 15*d*), the surviving rib vortices and some core streamwise vorticity form a stagnation point in the BP near the position of the forming vortex sheet (see figure 22). Note that the large regions of streamwise vorticity at the bottom of the domain in figure 22(*b*) are the surviving rib vortices. This quadrupole produces a persistent coherent strain that produces the thin sheet of spanwise vorticity in the same way that the cups were formed (see RM §4.3.1). Other thin sheets that form in the roller core are similarly produced by coherent strain in the BP, but the complexity of the core precludes associating these coherent strain regions with known structures. In the more complex HIGH2P flow described in §6, the formation of thin sheets and their secondary rollup is a prominent feature of the BP spanwise vorticity.

6. Multiple pairings

It was observed in §5.2 that if a mixing layer is sufficiently three-dimensional, a transition to turbulence can be initiated by a pairing. To allow such a transition to be completed, flows with two pairings have been simulated. In addition, we wish to determine if, for flows with weaker three-dimensionality, a transition might be triggered by the second pairing. This might be expected since the level of three-dimensionality increases after the first pairing (see §4.1). Three cases with different initial levels of three-dimensionality were simulated (LOW2P, MID2P and HIGH2P). LOW2P has an initial circulation comparable to that of LOW1P, HIGH2P has an initial

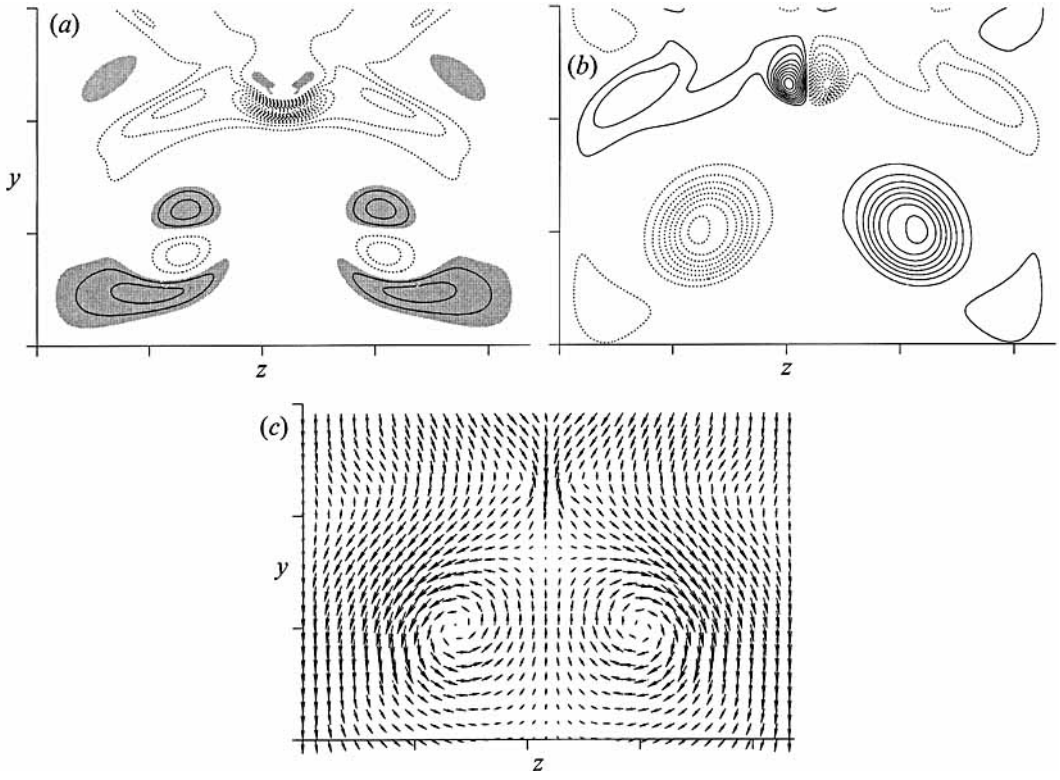

FIGURE 22. The HIGH1P flow in the (z, y)-plane passing through the vertical line in figure 15(*d*). (*a*) ω_z contours, (*b*) ω_x contours and (*c*) velocity vectors. The contour increment is ± 0.6, and in (*a*) regions of positive spanwise vorticity are shaded. The y-domain depicted is from -4 to -1.

circulation comparable to HIGH1P and MID2P is intermediate between these two (see table 2). For historical reasons, initial disturbances for these cases have different functional forms than those of the flows discussed in the previous sections. This was shown in Rogers & Moser (1991) to cause no qualitative, and only slight quantitative, differences in the flow evolution.

6.1. *Weakly three-dimensional double pairings*

Since the LOW2P flow has initial three-dimensionality similar to that of LOW1P, it is expected to agree equally well with linear analysis (see §5.1) through the first pairing. This is indeed the case as can be seen in figures 23(*a*) and 23(*b*), where the normalized three-dimensional amplitude A^*_{3D} and the normalized circulation Γ^*_x are plotted. Note, however, that by the time of the second pairing, LOW2P shows significant deviations from the linear evolution, despite its initially weak three-dimensionality. In LOW2P, the rib collapse criterion is not satisfied until $t \approx 25$ (figure 23*c*), well after the first pairing, despite the fact that collapse of the ribs is one of the first nonlinear processes to occur (see RM). The MID2P flow exhibits slightly greater departures from the predictions of the linear analysis, but is still qualitatively similar to LOW1P. The relatively weak three-dimensionality of these two flows is in strong contrast to the large departures from the linear analysis observed in the HIGH2P flow.

When compared to the structure of the linear perturbations, the structure of the vorticity field in LOW2P shows differences similar to those observed in LOW1P (e.g. figure 12). In particular, the vertical extent of the rib streamwise vorticity in the

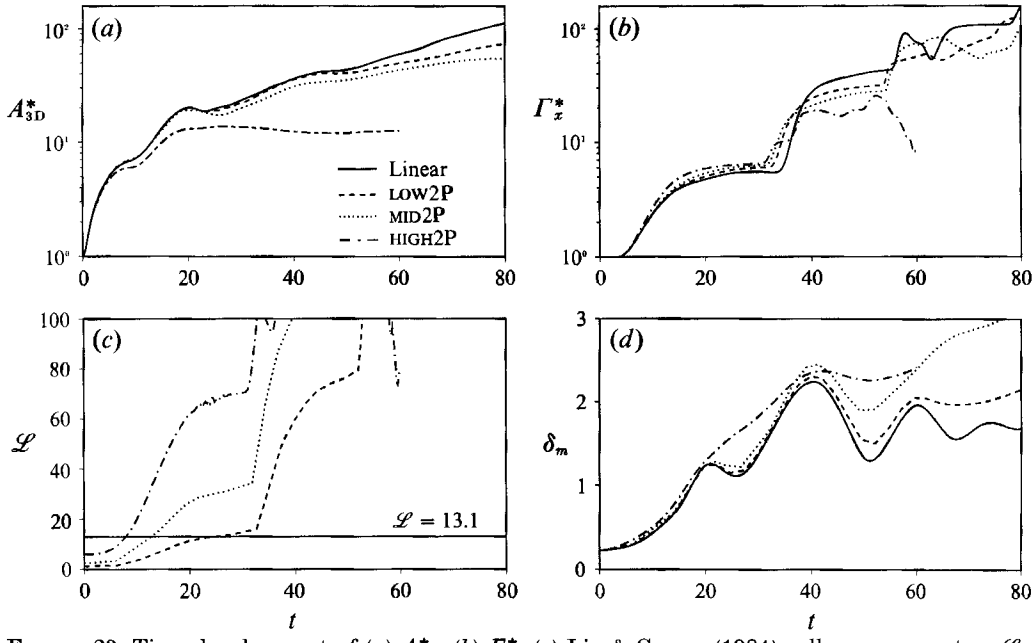

FIGURE 23. Time development of (a) A^*_{3D}, (b) Γ^*_x, (c) Lin & Corcos (1984) collapse parameter, $\mathscr{L}$, and (d) momentum thickness, δ_m. The two-dimensional base flow for the linear results is 2D2PωG. Note $\mathscr{L} = 0$ for linear analysis and the curve labelled linear in (d) is for the base flow.

braid region is greater as a result of the collapse of the ribs and the thin filaments of ω_z^{3D} away from the roller core are absent (resulting in reduced levels of W_{z3D} when compared to the linear results). These effects are even more pronounced in the MID2P flow.† Notably absent from LOW2P are the isolated thin shear layers that formed in HIGH1P and led to secondary Kelvin–Helmholtz rollups.

The initial three-dimensionality of MID2P is approximately 2.5 times weaker than HIGH1P or HIGH2P. As a consequence, transition is not initiated at the first pairing of MID2P. However, the three-dimensionality of MID2P increases by a factor of two or more between the first and second pairings, as measured by A_{3D} and Γ_x (figure 23). Thus transition could conceivably be initiated at the second pairing. Contours of spanwise vorticity in both the BP and the RP of MID2P at $t = 39.1 \approx \tau_{p2}$ and $t = 54.7 \approx \tau_{s2}$ are shown in figure 24. While some of the features in these figures show some similarity to those of the HIGH1P flow shown in figures 15 and 16 (e.g. the formation of some thin filaments of spanwise vorticity in the BP), MID2P is clearly not undergoing a transition to small-scale turbulence at this time. There is no indication of secondary rollups forming on the thin sheets of spanwise vorticity and the spanwise vorticity in the RP remains fairly well organized, with relatively few positive regions.

There are several possible reasons for the lack of transition in MID2P at the second pairing. First, the aspect ratio of the three-dimensional disturbances (ratio of spanwise scale to streamwise scale of the flow) is a factor of two smaller at the second pairing than at the first pairing because no spanwise scale change has been allowed. This imposed small aspect ratio could inhibit the transition (although it is shown in Moser & Rogers 1992 that the flow evolution changes very little in a spanwise domain four times as large unless strong $(0, \beta)$ subharmonics are included in the initial

† A direct comparison of the vorticity contours at τ_{s2} for MID2P, LOW2P, and the corresponding linear results can be found in figure 35 of Moser & Rogers (1992).

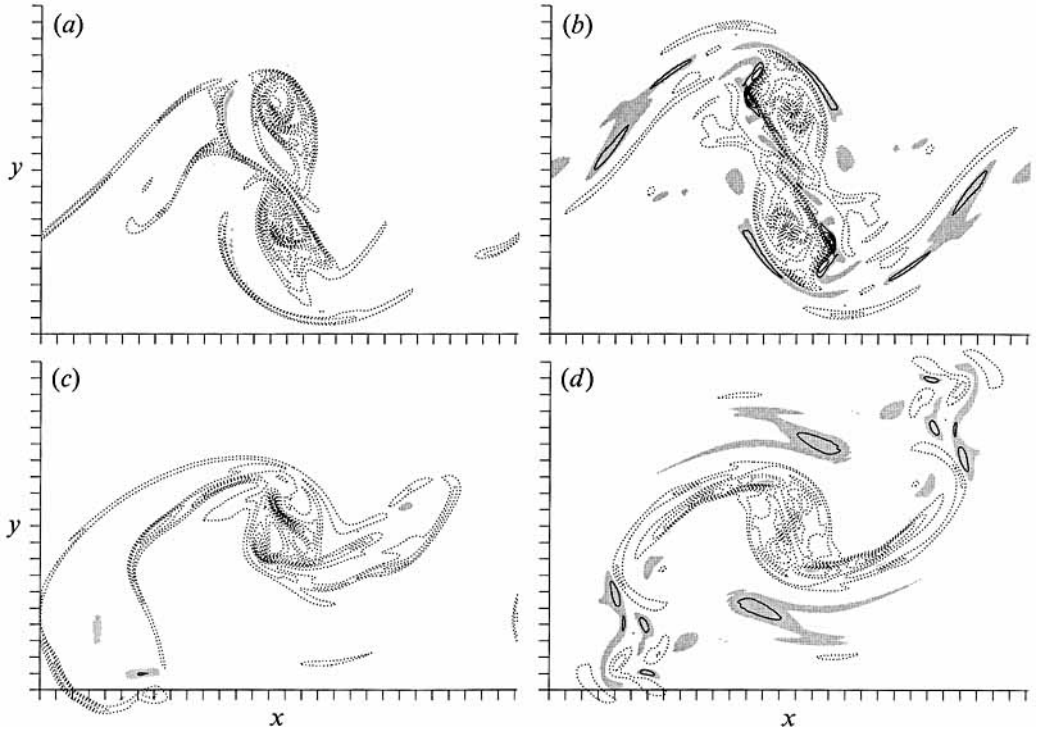

FIGURE 24. Contours of ω_z for MID2P in (*a*, *c*) the BP and (*b*, *d*) the RP at (*a*, *b*) $t = 39.1 \approx \tau_{p2}$ and (*c*, *d*) $t = 54.7 \approx \tau_{s2}$. The contour increment is ± 0.3. In this and subsequent similar figures areas of positive spanwise vorticity are shaded and negative contours are dotted.

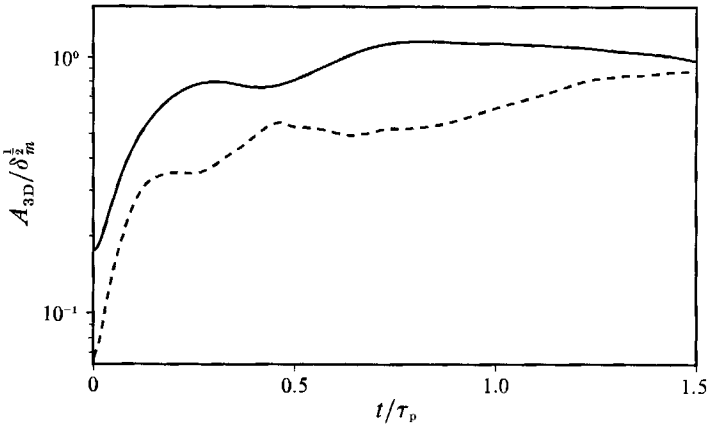

FIGURE 25. Time development of A_{3D}/δ_m^1 as a function of t/τ_p, for HIGH1P (——) and MID2P (----), where τ_p is τ_{p1} for HIGH1P and τ_{p2} for MID2P.

condition). Second, the three-dimensional amplitude A_{3D} is not a particularly good basis for comparison when the thicknesses of the mixing layers being compared are substantially different (e.g. HIGH1P at τ_{p1} versus MID2P at τ_{p2}). This is because there is an implied lengthscale in the definition of A_{3D} (see §2.2). A better measure in this case is A_{3D}/δ_m^1, which is plotted in figure 25 for MID2P and HIGH1P (the momentum thickness for HIGH1P and MID2P is plotted in figures 13*c* and 23*d* respectively). By this measure, the three-dimensionality of MID2P at τ_{p2} is a factor of 1.8 weaker than

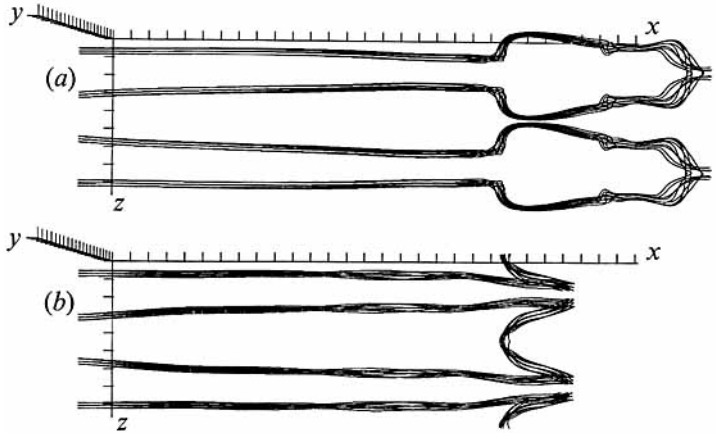

FIGURE 26. Top view of vortex lines that pass through or near the symmetry points in the surviving ribs for MID2P at (*a*) $t = 59.7$ and (*b*) $t = 65.0$. The domain has been periodically extended in the spanwise direction to show two pairs of ribs.

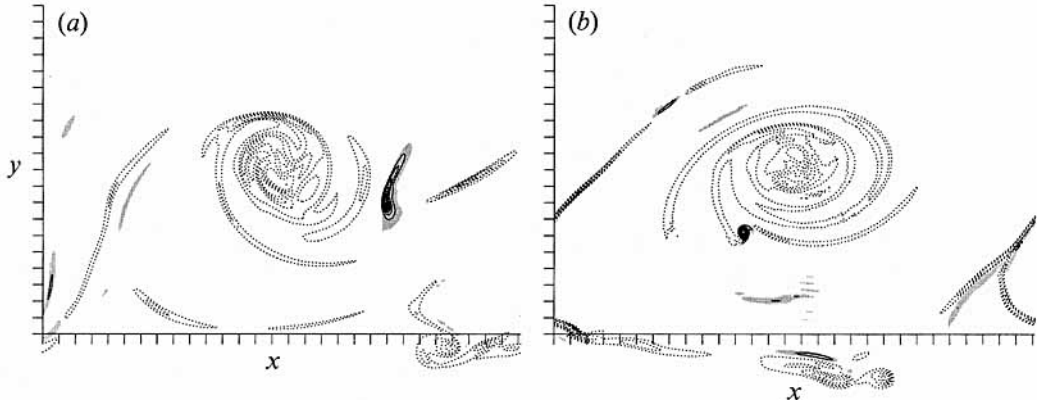

FIGURE 27. Contours of ω_z in the BP of MID2P at (*a*) $t = 65.0$ and (*b*) $t = 76.1$. Vortex lines shown in figure 26(*b*) pass through the region of intense positive vorticity in (*a*). The contour increment is ± 0.3 and the peak level of positive ω_z is 2.80 in (*a*) and 4.53 in (*b*).

that of HIGH1P at τ_{p1}. Finally, there may be some subtle difference between MID2P and HIGH1P due to the fact that MID2P has undergone a previous pairing. For example, in MID2P the roller cores have already paired once and therefore do not have the simple cup structures of unpaired rollers.

The MID2P flow is sufficiently three-dimensional for the rib vortex lines to be pulled all the way over the double-paired roller. This is illustrated in figure 26. As in HIGH1P, the rib vortex lines become distorted and are brought together with those of neighbouring ribs, allowing them to viscously reconnect. This has started to occur in figure 26(*a*) ($t = 59.7$). Note that the reconnection does not pinch off the heads of the hairpin vortices as was the case in HIGH1P. Instead, each rib reconnects with its other neighbour (figure 26*b*), which makes the heads of the resulting hairpins have spanwise vorticity of opposite sign (positive). The sense (or direction in z) of the rib vortex lines has thus been reversed. This reconnection results in a region of strong positive spanwise vorticity in the BP (figure 27). This positive vorticity is sheet-like at $t = 65.0$, but by $t = 76.1$ it is concentrated in a very compact 'roller'. The rib vortex line reconnection depicted in figure 26 is neither the first nor the last to occur in MID2P. At $t \approx 35$ (before the reconnection shown in figure 26), the rib vortex lines

reconnect as in HIGH1P, preserving the sense of the rib vortex lines. After the reconnection shown in figure 26, further reconnections occur, some of which change the sense in the tip region connecting the ribs and some of which preserve it.

6.2. *Highly three-dimensional double pairing*

As with HIGH1P, transition to small-scale turbulence is initiated at the first pairing (τ_{p1}) in HIGH2P. This can be observed in figures 28 and 29, where spanwise vorticity in the BP and RP of HIGH2P at four times (two of which are within the period illustrated in figures 15 and 16) are shown. Clearly, the same interaction of the cups in the pairing rollers is occurring, leading to the formation of thin shear layers, secondary rollups in the BP, and small-scale granularity in the RP (see §5.2). As the second pairing proceeds, the complex transitioning rollers are brought together. The structures in each roller can then interact, increasing the complexity of the double-paired roller. By $t = 39.1 \approx \tau_{p2}$ (figures 28*c* and 29*c*), the prepairing structure is no longer discernible. Thin sheets and secondary rollups in the BP and small-scale granularity in the RP, which characterize the flow at the first pairing, are also present at the second pairing. Later ($t = 52.1$, see figures 28*d* and 29*d*), secondary rollups continue and there is enhanced turbulence activity in the braid region, especially in the RP, while the turbulence in the core appears to be decaying.

The onset of turbulence is accompanied by the continuous entry of spanwise vorticity into the braid region (see figures 28 and 29), even before the second pairing. Thus, the process described in §3 by which pairing leads to re-entry of spanwise vorticity into the braid region is no longer relevant. There is no τ_{s2} in this case (see table 2). Also, since the braid region is turbulent, the circulation Γ_x can no longer be interpreted as the rib circulation.

As would be expected for a turbulent flow, many features of HIGH2P are qualitatively different from those of non-transitional flows. For example, a comparison of the spanwise vorticity of HIGH2P and MID2P at $t = 39.1 \approx \tau_{p2}$ (see figures 24, 28, and 29) reveals no similarity; HIGH2P is clearly turbulent while MID2P is not. The structures of the passive scalar fields present in these flows are also qualitatively different (figure 30). Scalar interfaces in HIGH2P are highly distorted with many small-scale features, while those in MID2P are smooth and regular. This suggests that a flow visualization of HIGH2P based on passive markers would appear turbulent. There has also been more molecular mixing of the scalar in the HIGH2P flow than in MID2P (see §7). Finally, the presence of turbulence produces a steadier growth of the mixing layer than in the non-transitional flows (see figure 23*d*). The oscillations in the thickness of the layer (caused by the pairings) have been largely eliminated, consistent with the monotonic growth expected of a fully turbulent layer. The characteristics of post-transitional turbulent mixing layers will be examined further in §7.

The flows discussed here and in §5 were precluded from undergoing a spanwise scale change because the largest possible spanwise wavelength corresponded to $\beta = 1$. The extent to which these simulations are affected by this constraint is therefore of great interest. Our main concern is how robust the results of §§5 and 6 are. That is, whether low-amplitude spanwise subharmonic modes produce any large changes in the flow evolution. To test this, two simulations (WMID2P and WHIGH2P, see table 2) with weak spanwise subharmonics were examined. Without the spanwise subharmonics, the WMID2P and WHIGH2P flows would be identical to the MID2P and HIGH2P flows, respectively. A comparison of WMID2P with MID2P and of WHIGH2P with HIGH2P thus allows one to determine the extent to which the constraints on spanwise scales

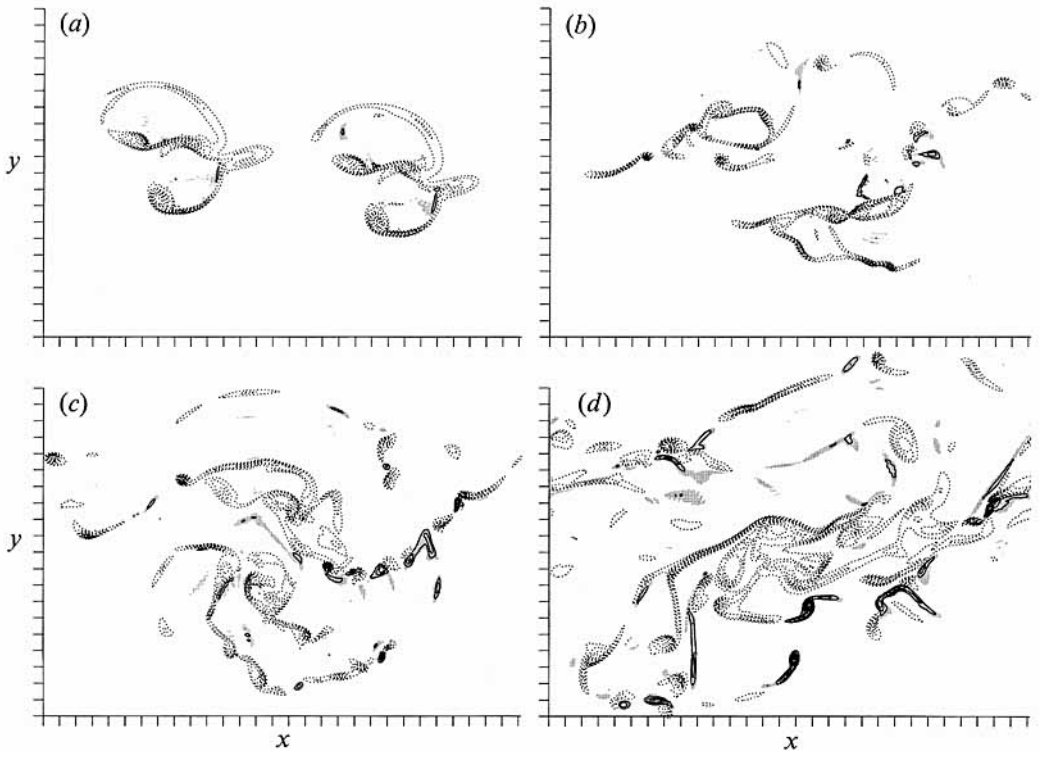

FIGURE 28. Contours of ω_z in the BP of HIGH2P at (*a*) $t = 19.1 \approx \tau_{p1}$, (*b*) $t = 31.9 \approx \tau_{s1}$, (*c*) $t = 39.1 \approx \tau_{p2}$ and (*d*) $t = 52.1$. The contour increments are (*a*) ± 0.6, (*b*) ± 0.8, (*c*) ± 0.5, and (*d*) ± 0.3.

in MID2P and HIGH2P are modifying the flow. Results of such a comparison indicate that the lack of spanwise subharmonics results in very little difference in the flow evolution (Moser & Rogers 1992). The amplitudes A_{s0} and A_{3D} agree well throughout the flow development, with A_{3D} differing by at most 6% even up to $t = 60$. Comparisons of flow field contour plots lead to the same conclusion. These results indicate that a spanwise scale change triggered by weak spanwise subharmonics is slow (Rogers & Moser 1993). Thus, strong spanwise subharmonics are needed for flow evolution to vary significantly from that discussed above.

7. Character of the post-transition flow

Several of the flows discussed in the preceding sections undergo a transition to turbulence. However, most of these were constrained in some artificial way. For example HIGH2P was constrained by the exclusion of spanwise subharmonics and the imposition of symmetries in the initial condition. While these constraints aided in the analysis of the transition process, they produce an unnatural turbulence. One case (TURB2P) was designed to eliminate all symmetries and most constraints. The disorder in the resulting flow is similar to that in experimental mixing layers. For example, passive scalar contours in the MP are similar to the flow visualization pictures of Bernal & Roshko (1986). In this section, the character of this turbulence is documented to provide a basis for comparisons with experimental measurements and future simulations begun from turbulent initial conditions. The flow at $t = 39.8$

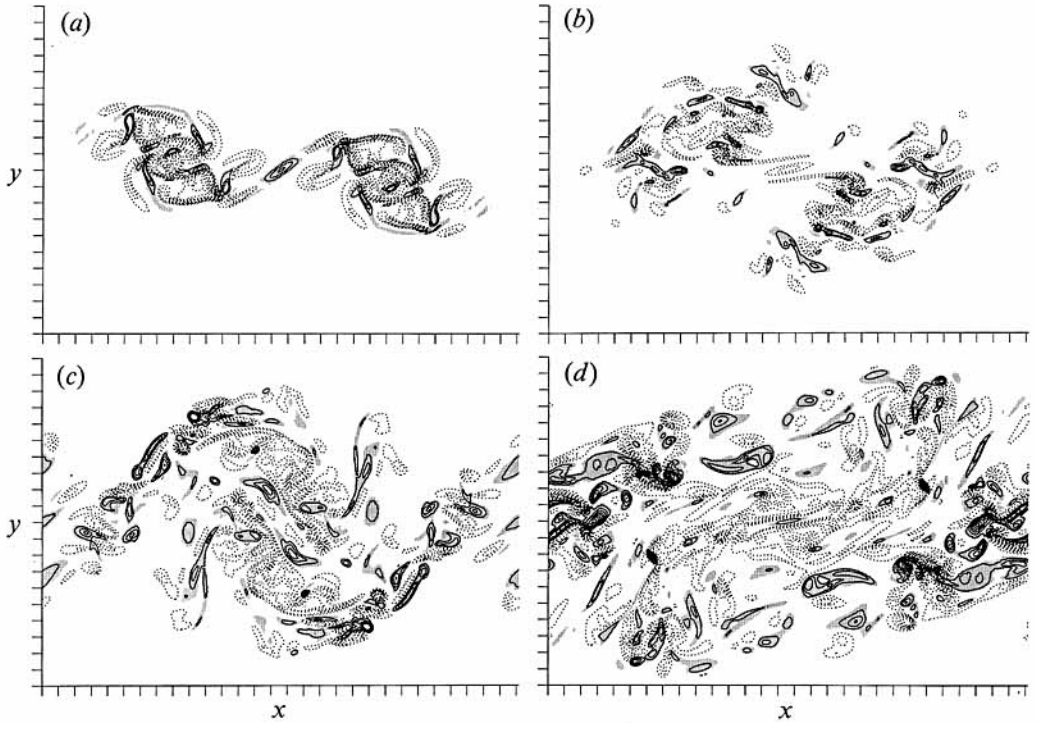

FIGURE 29. Contours of ω_z in the RP of HIGH2P at (*a*) $t = 19.1 \approx \tau_{p1}$, (*b*) $t = 31.9 \approx \tau_{s1}$, (*c*) $t = 39.1 \approx \tau_{p2}$ and (*d*) $t = 52.1$. The contour increments are (*a*) ± 0.6, (*b*) ± 0.8, (*c*) ± 0.5, and (*d*) ± 0.3.

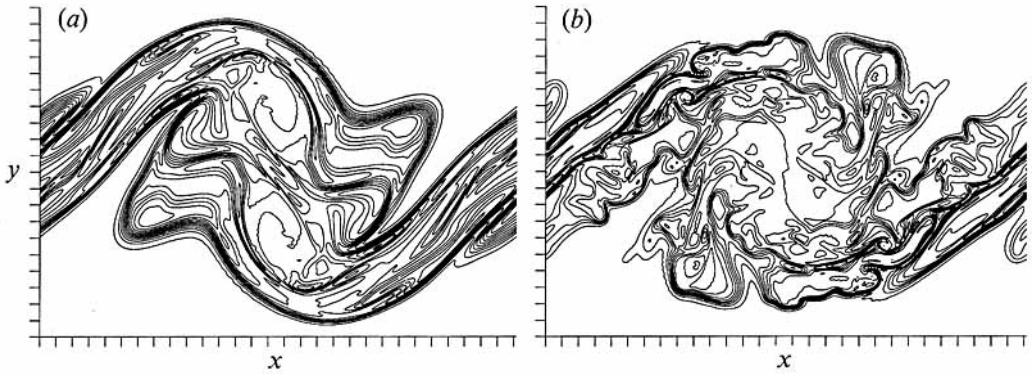

FIGURE 30. Contours of the passive scalar in the BP of (*a*) MID2P and (*b*) HIGH2P at $t = 39.1 \approx \tau_{p2}$. The contour increment is 0.08, from 0.02 (bottom) to 0.98 (top).

is chosen for this purpose because it contains 'healthy turbulence' and yet is before the second pairing at $\tau_{p2} = 47.1$ and is therefore far from being oversaturated. It is thus not affected by the absence of a further pairing.

The TURB2P flow undergoes a transition similar to that described in §6.2 for the HIGH2P flow. However, there is a subtle difference. Because of the strong subharmonic streamwise-invariant disturbances and their relative phasings, the ribs do not remain at fixed locations in the braid region. Consequently, well-defined 'rib

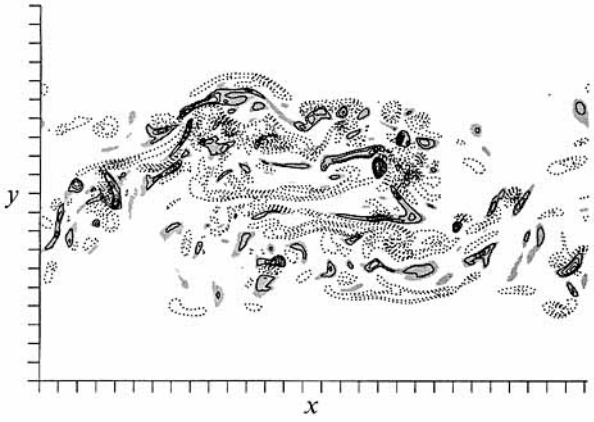

FIGURE 31. Contours of ω_z in the $z = 0$ (x, y)-plane at $t = 39.8$ in TURB2P. The contour increment is ± 0.5.

planes' and 'between-ribs planes' do not exist. The distinction between higher-order rollups of thin vortex sheets in the BP's and the granular patterns in the RP's is thus absent. The flow appears to contain a combination of both these features at all spanwise locations (see figure 31).

While contour plots of ω_z in the HIGH2P (figures 28 and 29) and TURB2P (figure 31) flows are qualitatively similar (with the above noted exception regarding the RP and BP features), the x, z (horizontal) planes appear significantly more 'turbulent' in TURB2P. Much of the increased complexity is due to the elimination of the symmetries (10) and (11). Vorticity contours in the centreline (x, z)-plane of the TURB2P flow are shown in figure 32 at times before and after the transition. The loss of regularity is obvious. (Note that there is still some evidence of engulfed ribs at $x = \frac{1}{2}L_x$ in figure 32*d*.)

The y-dependence of several horizontally averaged statistics is shown in figure 33. Both the mean velocity and mean scalar profiles are roughly symmetric around the layer centreline. The mean velocity ($\bar{U}$) is almost an error function (an error function of the same thickness is plotted in figure 33*a* for reference). The mean scalar ($\bar{T}$) profile is more nearly piecewise-linear. This suggests that a constant-eddy-viscosity model might be adequate for the transport of momentum, but not of the scalar. At this time ($t = 39.8$) both mean gradients are negligible beyond $|y| \approx 8$.

The r.m.s. velocity fluctuations (u', v', and w') and the Reynolds stress ($-\overline{uv}$) are shown in figure 33(*b*). At $t \approx 10$ (not shown), all r.m.s. velocities have a well-defined single peak at the centreline. By $t = 39.8$, however, they are approximately constant over the central portion of the mixing layer (about $-4 \leqslant y \leqslant 4$). The r.m.s. velocity fluctuations all decay slowly in y. This is due to the slowly decaying potential velocity fluctuations. Two-dimensional fluctuations dominate the potential velocity far from the vortical part of the layer, resulting in a lower level of w' compared to u' and v' for large y. The potential velocity fluctuations do not contribute to the Reynolds stress ($-\overline{uv}$), thus the Reynolds stress decays rapidly in y.† Like the r.m.s. velocities, the r.m.s. vorticities (denoted by ω_i' and shown in figure 33*d*) are roughly constant over the region $-4 \leqslant y \leqslant 4$ (profiles are even flatter at later times) after exhibiting single peaks at the centreline early in the layer development.

† The scalar fluctuations, the vorticity fluctuations, and the scalar fluxes also do not exhibit slowly decaying potential tails. All these quantities are essentially zero where the mean gradient is zero.

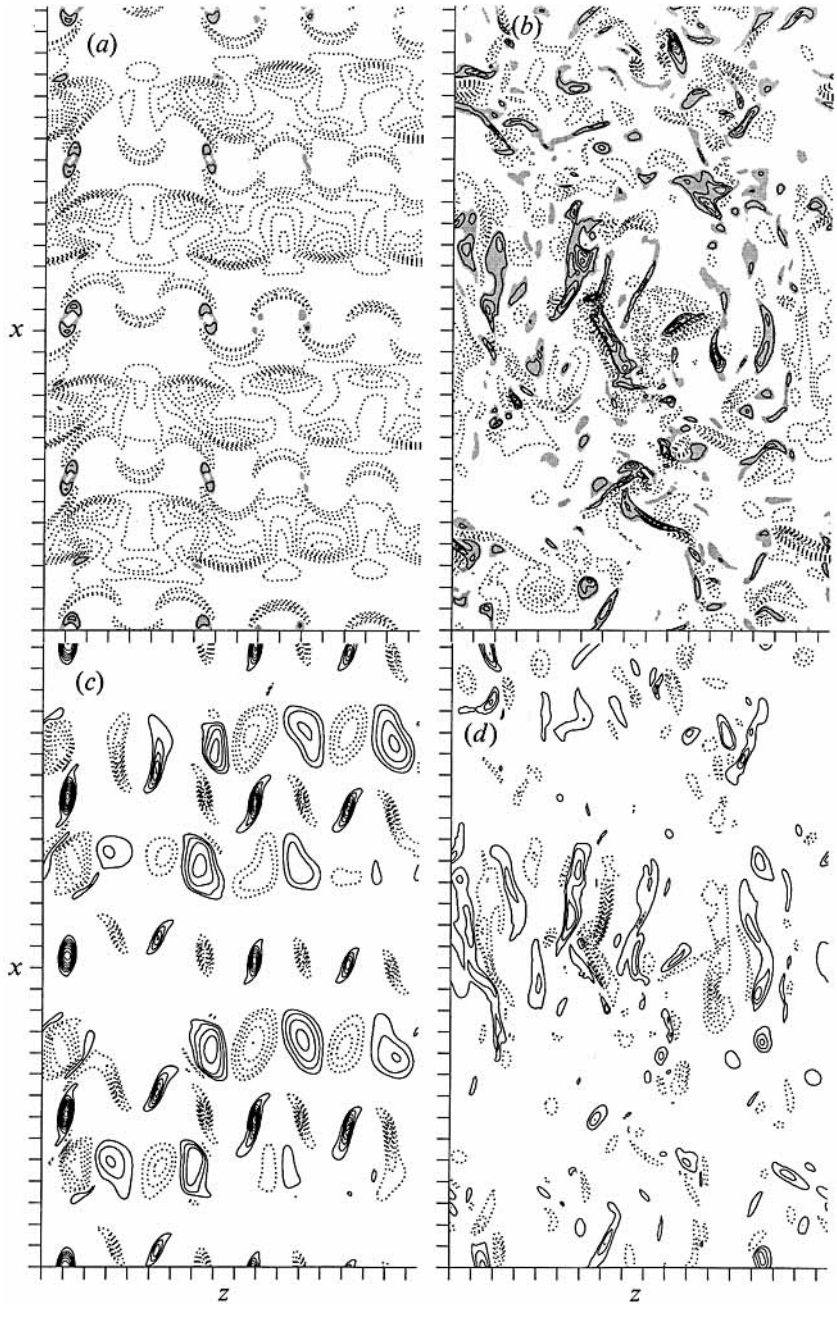

FIGURE 32. Contours of (*a*, *b*) ω_z and (*c*, *d*) ω_x in the centreline (z, x)-plane of the TURB2P flow at (*a*, *c*) $t = 11.7$ and (*b*, *d*) $t = 39.8$. The contour increment is ± 0.5 except in (*d*), where it is ± 1.0. Shaded regions indicate regions of positive ω_z (opposite in sign to the mean vorticity).

At $t = 39.8$, the Reynolds stress correlation coefficient $-\overline{uv}/(u'v')$ is just over 0.6 in the central portion of the layer. Later in time ($t = 50$), $-\overline{uv}$ changes sign over at least part of the layer (the middle at this time). This is associated with the completion of the second pairing ($\tau_{p2} = 47.1$). The reversal in sign of the Reynolds stress implies a counter-gradient momentum flux and is accompanied by a reduction in the

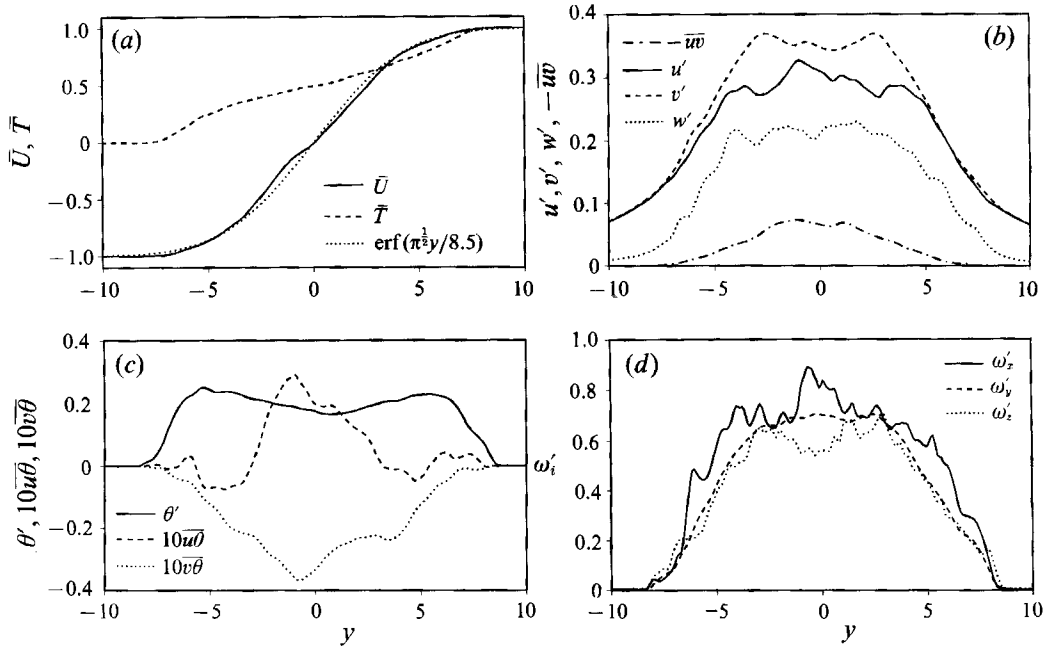

FIGURE 33. Profiles in y of various x, z averaged statistics for TURB2P at $t = 39.8$.

momentum thickness. It has been observed in other temporally developing (e.g. Riley & Metcalfe 1980; Metcalfe *et al.* 1987) as well as forced spatially developing (Oster & Wygnanski 1982; Lowery & Reynolds 1986; Lele 1989) mixing layers and is particularly prevalent in two-dimensional flows. Riley & Metcalfe and Metcalfe *et al.* attributed this change in sign to oversaturation. While it is true that the first pairing (unless substantially delayed) will prevent this change in sign of the Reynolds stress after the rollup, further pairings do not, in general, happen fast enough to eliminate a period of counter-gradient momentum flux after each pairing. Strong three-dimensionality can change this, however, and both the TURB2P and WHIGH2P flows do not exhibit such a change in sign after the *first* pairing (as the WMID2P flow does). It is unclear whether the change in sign observed in all three of these flows after the *second* pairing could be prevented by a third pairing.

The r.m.s. scalar fluctuation profile (note θ is used here for $T - \bar{T}$ and θ' is its r.m.s. value) is double-peaked (figure 33*c*), a feature that becomes more pronounced after the first pairing. Because of the mean shear, the turbulent scalar flux vector has both streamwise and vertical components ($\overline{u\theta}$ and $\overline{v\theta}$), even though there is no streamwise mean scalar gradient. The correlation coefficients $\overline{u\theta}/(u'\theta')$ and $\overline{v\theta}/(v'\theta')$ at $t = 38.9$ are roughly 0.4 and -0.5, respectively.

The profiles of $\bar{\epsilon}$, the x, z averaged dissipation rate of turbulent kinetic energy, at $t = 39.8$ in TURB2P and at $t = 40.1$ in WMID2P are shown in figure 34(*a*). The time evolution of the y-integral of these profiles (ϵ_t) is shown in figure 34(*b*) for the same two flows. The presence of many small-scale structures in the TURB2P flow (e.g. figures 32*b* and 32*d*) results in a significantly higher rate of kinetic energy dissipation. As a result, the integrated turbulent kinetic energy is smaller in TURB2P than in WMID2P after τ_{p1}. Note that in WMID2P the 'production' of turbulent kinetic energy actually becomes negative for a period after each pairing. Thus while the kinetic energy is roughly constant in TURB2P after $t = \tau_{p1}$, it increases and oscillates in WMID2P, remaining above the TURB2P level for $t > \tau_{p1}$.

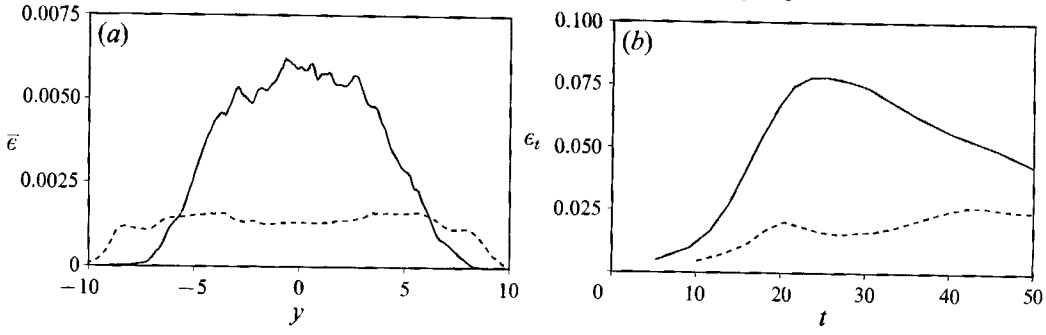

FIGURE 34. Dissipation rate of turbulent kinetic energy for TURB2P (——) and WMID2P (----). (*a*) Profiles in y of x, z averaged dissipation rate at $t = 39.8$ for TURB2P and at $t = 40.1$ for WMID2P. (*b*) Time evolution of y-integrated dissipation rate.

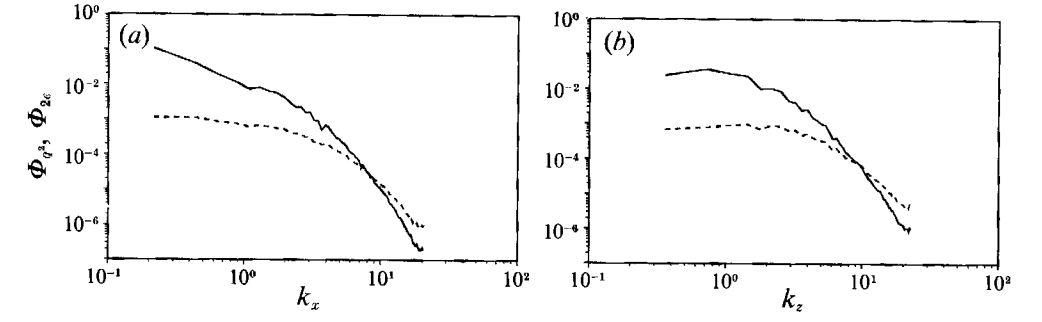

FIGURE 35. One-dimensional spectra of q^2 (——) and 2ϵ (----) in the (*a*) streamwise and (*b*) spanwise directions at the centreline of the layer for $t = 39.8$ for TURB2P.

The quantities shown above can be used to form a turbulent timescale $\overline{q^2}/\bar{\epsilon} = (\overline{u'^2}+\overline{v'^2}+\overline{w'^2})/\bar{\epsilon}$. This timescale is roughly constant in the core of the layer and is about 50 at $t = 39.8$. The turbulence Reynolds number, $Re_T = \overline{q^2}^2/(\bar{\epsilon}\nu)$, is about 3000 in the middle of the layer at this time.

One-dimensional spectra of q^2 and 2ϵ at $y = 0$ in TURB2P at $t = 39.8$ are shown in figure 35. These spectra indicate that the flow is well resolved since there is at least a two decade falloff in the dissipation spectra. Also, the fact that this is a low-Reynolds-number turbulent flow is evident in the lack of a discernible inertial range. Finally, it is clear that the streamwise domain size constrains the flow evolution, since the streamwise q^2 spectrum does not plateau at low wavenumbers. This is expected since $t = 39.8$ is well into the second and final pairing in this flow.

In addition to an increased rate of kinetic energy dissipation, the small-scale turbulence provides more thorough 'mixing'. A zero-heat-release fast chemical reaction can be studied using the passive scalar carried in the simulations (Burke & Schumann 1928; Zeldovich 1951; Toor 1962). The ratio of the amount of reaction product to the reaction product that would be present if there were no scalar fluctuations is a measure of the degree of scalar mixing (Konrad 1976). This ratio is denoted by $\mathscr{M}$ and is given by

$$\mathscr{M} = \frac{\int_{-\infty}^{\infty} \overline{\mathscr{P}(T(t))} - \mathscr{P}(\bar{T}(t=0))\,\mathrm{d}y}{\int_{-\infty}^{\infty} \mathscr{P}(\bar{T}(t)) - \mathscr{P}(\bar{T}(t=0))\,\mathrm{d}y}, \tag{16}$$

where $\mathscr{P}(T) = 1-|2T-1|$ is the product concentration, an overline indicates the

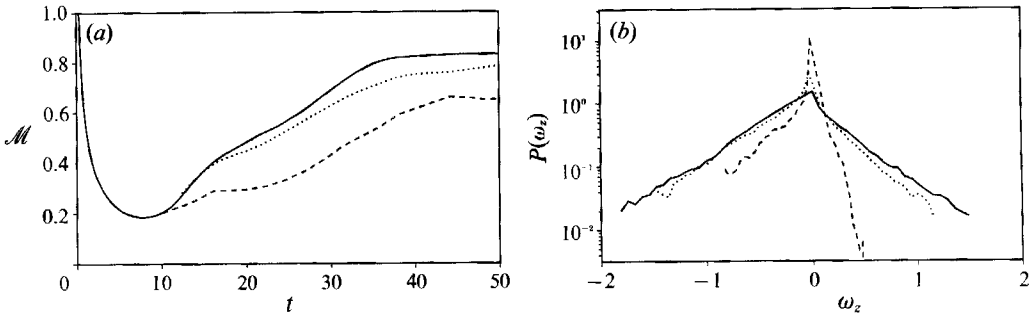

FIGURE 36. Comparisons between the WMID2P (----), WHIGH2P (· · · · · ·), and TURB2P (——) flows. (*a*) Time development of the 'mixedness' parameter $\mathscr{M}$. (*b*) Probability density function of ω_z at the centreline of the layer for TURB2P at $t = 39.8$, WMID2P at $t = 40.1$, and WHIGH2P at $t = 39.9$.

average over x and z, and the second term in each integrand eliminates the contribution of the initial scalar profile. Because $\mathscr{M}$ is a ratio, it provides a fair comparison of mixing in layers of different thickness. In figure 36(*a*) the evolution of this ratio for TURB2P, WHIGH2P, and WMID2P is shown (two of these curves have been shown in Moser & Rogers 1991). Note that the ratio is initially 1.0 since there are no scalar fluctuations at $t = 0$. The late-time plateau level of the transitional TURB2P flow is 0.18 greater than that of the non-transitional WMID2P flow. This difference is close to the value of 0.15 measured by Konrad (1976) in his experiments at similar Schmidt number (0.7 compared to our 1.0).

The probability density function (p.d.f.) of ω_z is qualitatively different in the transitional and the non-transitional flows. As can be seen in figure 36(*b*), WMID2P, WHIGH2P, and TURB2P all exhibit roughly exponential decay of $P(\omega_z)$ as $|\omega_z|$ becomes large. There are, however, two distinct differences between the transitional and non-transitional flows. In the non-transitional case (WMID2P), there is little positive ω_z (opposite in sign to the mean vorticity) and there are significant amounts of irrotational fluid (or at least fluid with $\omega_z \approx 0$) near the centreline of the layer. In contrast, the p.d.f. of ω_z in the TURB2P flow is more symmetric and has a much smaller peak at $\omega_z = 0$. The p.d.f. for the WHIGH2P flow is intermediate in both these respects. These results suggest a possible transition criterion based on the level of positive ω_z present in the flow. Such a criterion was proposed by Moser & Rogers (1991).

8. Summary and discussion

The simulations described in the previous sections provide a detailed description of three-dimensional mixing layers undergoing pairings of the primary Kelvin–Helmholtz rollers and, in some cases, transition to turbulence. The early time evolution through the first Kelvin–Helmholtz rollup was described in RM (summarized here in the Appendix). In this section, the effects of pairing on three-dimensional mixing layers are summarized and the results are compared with conclusions reached in earlier studies.

8.1. *Two-dimensional mixing layers and three-dimensional small disturbances*

Several important features of three-dimensional mixing-layer evolution are governed by the development of the two-dimensional Kelvin–Helmholtz rollers and can therefore be understood in the context of a two-dimensional flow with a three-

dimensional small disturbance. The process of pairing pulls the rollers away from the surviving braid region. If initiated soon enough this prevents oversaturation (described in RM) and the associated re-entry of spanwise vorticity into the surviving braid region. Pairing therefore prevents (or delays) the rapid, apparently exponential, growth of three-dimensionality associated with oversaturation. As the pairing is completed, spiral arms of vorticity are ejected from the paired roller, and re-enter the surviving braid region. This re-entry of vorticity results in a period of rapid growth of three-dimensionality, which is arrested as the spanwise vorticity is again drawn out of the braid region. Unlike oversaturation, the re-entry of spanwise vorticity associated with the spiral arms cannot be suppressed by further pairings. Thus after each pairing there is a period of disturbance growth resulting in an increase in three-dimensionality by an approximately constant factor for each pairing (see §4.1). Once pairings have ceased, the final paired roller eventually oversaturates as described in RM, with a resulting exponential growth of three-dimensionality.

The prevention of oversaturation by pairing is the reason that pairing has been observed to inhibit the growth of three-dimensionality (Metcalfe *et al.* 1987; Huang & Ho 1990). Oversaturation results in spanwise vorticity entering the braid region and remaining there. Three-dimensional perturbations then grow continuously. In contrast, continued pairings result in discrete periods of disturbance growth as described above. The time between pairings, and therefore the time between these periods of growth, approximately doubles with each pairing. This results in algebraic long-term growth of three-dimensionality rather than the exponential growth that occurs during oversaturation.

If pairing is not initiated fast enough, oversaturation and its associated exponential growth of three-dimensionality can occur prior to the pairing. Because the growth of three-dimensionality during and after the pairing is similar for all pairings, delayed pairing results in more three-dimensionality. This is relevant to forced experimental mixing layers in which forcing can suppress pairing.

The results of RM suggested that the translative instability responsible for the growth of three-dimensionality in an oversaturated mixing layer is not associated with an isolated portion of the flow (i.e. braid region or core), since it produces continuous growth of both rib circulation and roller kinking. The growth of three-dimensionality in a pairing mixing layer prior to oversaturation is also not localized to a particular region of the flow. As the spiral arms introduce spanwise vorticity into the braid region, growth occurs there preferentially. Later the roller becomes more three-dimensional until a rough equilibrium is reached. At this time, disturbance growth stops until the next spiral arms initiate another period of growth. Clearly, the instability should be considered to be one of the flow as a whole.

It is apparently impossible for a two-dimensional mixing layer to undergo a sequence of self-similar pairings (i.e. pairings in which the paired roller is similar to the original unpaired rollers). At sufficiently high Reynolds numbers, or after sufficiently many pairings, vorticity does not diffuse fast enough to maintain a self-similar configuration. Thus with each pairing the region of vorticity concentration in the roller gets smaller relative to the distance between rollers.

8.2. *Highly three-dimensional flows*

Pairing in a weakly three-dimensional mixing layer is well described by the linear evolution of a three-dimensional perturbation as discussed above. However, pairing in more strongly three-dimensional layers results in significant nonlinearities and, in some cases, the beginnings of the transition to turbulence. In §5 the details of the

initial portion of such a transition are described. In this case transition is triggered by a pairing in a flow that is significantly three-dimensional (i.e. contains strong 'cups' and collapsed 'ribs'), although still organized into a few large-scale structures. By the time the pairing is complete, the layer has become disorganized and the origins of many vortical structures can no longer be traced back to their organized prepairing counterparts. After the pairing, vortex stretching increases the complexity of the flow. Remnants of the original rib vortices together with newly created vortices generate thin vortex sheets; these sheets are unstable and undergo higher-order rollups, further increasing the complexity of the flow by generating small scales. When this transitioning flow undergoes a further pairing, an apparently fully turbulent mixing layer results, which bears a strong resemblance to experimental turbulent mixing layers and shows many characteristics of turbulent flows in general (see §7).

The pairing-induced transition described in §5 has many characteristics in common with experimentally observed transition. The experiments of Huang & Ho (1990) also indicated that the timing of the transition was related to the occurrence of pairings and that the flow was fully turbulent by the completion of the second pairing. The small scales in their flow were found to first appear predominantly in the roller core at spanwise locations where ribs were located, consistent with the results presented here. Finally, the level of the mixedness parameter $\mathscr{M}$ (defined in (16)) in the transitional flows is about 0.18 higher than the corresponding level in flows that do not undergo transition. This increase is similar to the increase in mixedness observed experimentally (Konrad 1976).

Other possible transition mechanisms (besides the pairing-induced one considered above) also exist. In particular, a few simulations described in RM and Rogers & Moser (1993) that do not undergo any pairings appear to be transitional. In such flows transition results from either extremely large initial three-dimensional disturbances or from a long development in the oversaturated state. In the HIROLL flow of RM, the initial three-dimensional disturbance strength was four times that of the baseline ROLLUP case in RM and the HIGH1P simulation here. This initial level of three-dimensionality is so high that significant nonlinear behaviour results before the rollup is complete. By the time the flow reaches oversaturation it is apparently turbulent (RM, figure 25), with thin vortex sheets undergoing higher-order rollups in the between-ribs plane and small-scale granular vorticity structures in the rib plane. Transition, perhaps of a different character, can also result from long flow development after oversaturation. The PH$\frac{1}{4}\pi$0P flow discussed in Rogers & Moser (1993) does not undergo any pairings, is begun from three-dimensional disturbances of only moderate strength, and yet is also apparently turbulent by $t = 30.0$.

Finally, not all pairing mixing layers behave as those described in this paper. In particular, oblique subharmonic disturbances can lead to a variety of different features (e.g. ribs of alternating sign in the streamwise direction, hoops, and spanwise scale reduction, see Moser & Rogers 1992). Despite this, when these flows have well-defined collapsed rib vortices and undergo a pairing, a similar transition to turbulence is initiated.

Much of this work was begun in collaboration with visiting scientists at the 1988 Center for Turbulence Research Summer School Program. In particular, we are grateful for discussions with Professors C.-M. Ho, F. Hussain, and J. Riley. In addition, we have benefited from comparisons with the spatially developing mixing-layer work of Dr J. Buell, the compressible shear layer work of Professor S. K. Lele,

and Professor E. Broadwell's vast experience with experimental mixing layers. Helpful comments provided by Dr N. Mansour and Professor S. K. Lele on a draft of this paper are also appreciated. Some of the computations were performed on the NAS supercomputers at NASA Ames Research Center.

Appendix

The presentation of many of the results in this paper assumes familiarity with the evolution of three-dimensional Kelvin–Helmholtz rollups as presented in Rogers & Moser (1992) (RM). Here a summary of the results of RM is presented. This summary includes both a brief description of the vortical structures that develop as the layer rolls up and definitions of terms and quantities given in RM that will also be used here.

In RM a 'typical' rollup evolution that resulted from the standard set of initial conditions used here (see §2.2), as well as many other initial conditions, was identified. The typical Kelvin–Helmholtz rollup produces the well-known spanwise vortices (rollers) and the familiar array of predominately streamwise vortices (ribs) that extend from below one roller to above its downstream neighbour. The rib vortices alternate in sign in the spanwise direction and are roughly aligned with the extensional strain in the region between the rollers (the braid region). The ribs are formed from vortex lines that are kinked in the streamwise direction and become stretched by the extensional strain in the braid region. In the core of the rollers, vortex lines become kinked in the opposite direction, resulting in streamwise vorticity with sign opposite that in the rib at the same spanwise location. The combined strain produced by the ribs as they pass over the top (or under the bottom) of the roller and the oppositely signed roller streamwise vorticity alternately (in the spanwise direction) stretches and compresses the spanwise vorticity at the top and bottom of the roller. This results in cup-shaped regions (cups) of intense spanwise vorticity in the roller, these cups being located between the rib vortices and alternating from the top to the bottom of the roller in the span (see figure 14 of RM). The experiments of Nygaard & Glezer (1991) suggest that similar structures occur in experimental mixing layers. On the opposite side of the roller from each cup is a 'wisp' of weaker spanwise vorticity (see figure 15 of RM). This wisp contains the vortex lines that loop from one rib to its neighbour.

To a large extent, the strength of the cups and the degree of three-dimensionality in the mixing layer can be determined from the strength of the ribs. The best measure of the rib strength is the rib circulation, here denoted by Γ_x. It is defined as

$$\Gamma_x = \int_{-\infty}^{\infty}\int_{0}^{\lambda_z/2} \omega_x \,\mathrm{d}z\,\mathrm{d}y = -\int_{-\infty}^{\infty} v\,\mathrm{d}y\Big|_{z=0}^{\lambda_z/2}, \tag{A 1}$$

where $z = 0$ is taken to be one of the planes of symmetry defined in (10), that is a between-ribs plane (BP). Throughout this paper the rib circulation is measured at x-locations corresponding to the mid-braid plane (MP).† A superscript 0 and $*$ will be used to denote, respectively, the circulation at $t = 0$ and the circulation normalized by its value at $t = 0$. By manipulating the Navier–Stokes equations, the governing equation for Γ_x can be obtained (for simplicity the inviscid case is considered here):

$$\frac{\partial \Gamma_x}{\partial t} = \int_{-\infty}^{\infty} (u\omega_z)\,\mathrm{d}y\Big|_{z=0}^{\lambda_z/2} = \int_{-\infty}^{\infty} \left(u\frac{\partial v}{\partial x}\right)\mathrm{d}y\Big|_{z=0}^{\lambda_z/2}. \tag{A 2}$$

† Γ_x^{MP} was used to denote the MP circulation in RM.

Equation (A 2) implies that there must be spanwise vorticity in the MP for Γ_x to grow. Indeed in RM it was observed that the rib circulation stopped growing as the spanwise vorticity was drawn out of the braid region by the forming roller. It was then precluded from further growth until some event (oversaturation in RM) brought spanwise vorticity back into the MP. This is of great importance in the pairing of three-dimensional mixing layers (see §4).

The rib circulation is also important in determining whether the ribs collapse into compact nearly axisymmetric vortices as described by Lin & Corcos (1984). In RM it was found that the Lin & Corcos criterion was an accurate predictor of rib collapse in the mixing layer. A collapse parameter $\mathscr{L}$ was defined based on a curve fit to the curve in figure 9 of Lin & Corcos, resulting in the collapse criterion:

$$\mathscr{L} = \frac{\Gamma_x}{\nu^p (S\lambda_z^2)^{1-p}} > 13.1, \tag{A 3}$$

where $p = 0.6825$ is the curve fit parameter and S is the maximum two-dimensional (i.e. average in z) principal strain rate in the MP. Collapse of the ribs is a nonlinear phenomenon, and it was shown in RM to be one of the first three-dimensional nonlinearities to occur. It was also found that rib collapse was a prerequisite for the formation of strong cups as described above. Though cup formation is nonlinear, the mechanism leading to the strain that produces the cups is linear with respect to the two-dimensional evolving base flow (see §3.1 of RM).

Finally, two further definitions from RM are given here. One is that of the momentum thickness (δ_m) defined by

$$\delta_m = \frac{1}{4}\int_{-\infty}^{\infty} (1-\bar{U}^2)\,\mathrm{d}y. \tag{A 4}$$

The other is that of the mid-braid vorticity ($-\omega_b$). For mixing layers with negative mean vorticity (like those considered here), ω_b is the minimum (most negative) of the spanwise-averaged spanwise vorticity in the MP. The mid-braid vorticity is an indicator of the amount of spanwise vorticity in the braid region, which is a necessary ingredient for rib circulation growth as mentioned above.

REFERENCES

Bernal, L. P. 1981 The coherent structure of turbulent mixing layers. Ph.D. thesis, California Institute of Technology.

Bernal, L. P. & Roshko, A. 1986 Streamwise vortex structure in plane mixing layers. *J. Fluid Mech.* **170**, 499–525.

Breidenthal, R. 1981 Structure in turbulent mixing layers and wakes using a chemical reaction. *J. Fluid Mech.* **109**, 1–24.

Brown, G. L. & Roshko, A. 1974 On density effects and large structure in turbulent mixing layers. *J. Fluid Mech.* **64**, 775–816.

Buell, J. C. & Mansour, N. N. 1989 Asymmetric effects in three-dimensional spatially-developing mixing layers. In *Proc. Seventh Intl Symp. on Turbulent Shear Flows, Stanford University, Stanford, CA*, pp. 9.2.1–9.2.6.

Buell, J. C., Moser, R. D. & Rogers, M. M. 1992 A comparison of spatially and temporally developing mixing layers. (In preparation.)

Burke, S. P. & Schumann, T. E. W. 1928 Diffusion flames. *Ind. Engng Chem.* **20**, 998–1004.

Corcos, G. M. & Lin, S. J. 1984 The mixing layer: deterministic models of a turbulent flow. Part 2. The origin of the three-dimensional motion. *J. Fluid Mech.* **139**, 67–95.

CORCOS, G. M. & SHERMAN, F. S. 1984 The mixing layer: deterministic models of a turbulent flow. Part 1. Introduction and the two-dimensional flow. *J. Fluid Mech.* **139**, 29–65.

HERNAN, M. A. & JIMENEZ, J. 1982 Computer analysis of a high-speed film of the plane turbulent mixing layer. *J. Fluid Mech.* **119**, 323–345.

HO, C.-M. & HUANG, L.-S. 1982 Subharmonics and vortex merging in mixing layers. *J. Fluid Mech.* **119**, 443–473.

HO, C.-M. & HUERRE, P. 1984 Perturbed free shear layers. *Ann. Rev. Fluid Mech.* **16**, 365–424.

HUANG, L.-S. & HO, C.-M. 1990 Small-scale transition in a plane mixing layer. *J. Fluid Mech.* **210**, 475–500.

JIMENEZ, J. 1983 A spanwise structure in the plane shear layer. *J. Fluid Mech.* **132**, 319–336.

KELLY, R. E. 1967 On the stability of an inviscid shear layer which is periodic in space and time. *J. Fluid Mech.* **27**, 657–689.

KONRAD, J. H. 1976 An experimental investigation of mixing in two-dimensional turbulent shear flows with applications to diffusion-limited chemical reactions. *Internal Rep.* CIT-8-PU. Calif. Inst. Technol. Pasadena, CA.

KOOCHESFAHANI, M. M. & DIMOTAKIS, P. E. 1986 Mixing and chemical reactions in a turbulent liquid mixing layer. *J. Fluid Mech.* **170**, 83–112.

LASHERAS, J. C., CHO, J. S. & MAXWORTHY, T. 1986 On the origin and evolution of streamwise vortical structures in a plane, free shear layer. *J. Fluid Mech.* **172**, 231–258.

LASHERAS, J. C. & CHOI, H. 1988 Three-dimensional instability of a plane free shear layer: an experimental study of the formation and evolution of streamwise vortices. *J. Fluid Mech.* **189**, 53–86.

LELE, S. K. 1989 Direct numerical simulation of compressible free shear flows. *AIAA Paper* 89-0374.

LIN, S. J. & CORCOS, G. M. 1984 The mixing layer: deterministic models of a turbulent flow. Part 3. The effect of plane strain on the dynamics of streamwise vortices. *J. Fluid Mech.* **141**, 139–178.

LOWERY, P. S. & REYNOLDS, W. C. 1986 Numerical simulation of a spatially-developing, forced, plane mixing layer. *Dept. Mech. Engng Rep.* TF-26. Stanford University, Stanford, California.

MARTEL, C., MORA, E. & JIMENEZ, J. 1989 Small scales generation in 2-D mixing layers. *Bull. Am. Phys. Soc.* **34**, 2268.

METCALFE, R. W., ORSZAG, S. A., BRACHET, M. E., MENON, S. & RILEY, J. J. 1987 Secondary instability of a temporally growing mixing layer. *J. Fluid Mech.* **184**, 207–243.

MONKEWITZ, P. A. 1988 Subharmonic resonance, pairing and shredding in the mixing layer. *J. Fluid Mech.* **188**, 223–252.

MONKEWITZ, P. A. & HUERRE, P. 1982 Influence of the velocity ratio on the spatial instability of mixing layers. *Phys. Fluids* **25**, 1137–1143.

MOORE, D. W. & SAFFMAN, P. G. 1975 The density of organized vortices in a turbulent mixing layer. *J. Fluid Mech.* **69**, 465–473.

MOSER, R. D. & ROGERS, M. M. 1991 Mixing transition and the cascade to small scales in a plane mixing layer. *Phys. Fluids* A **3**, 1128–1134.

MOSER, R. D. & ROGERS, M. M. 1992 The three-dimensional evolution of a plane mixing layer Part 2: Pairing and transition to turbulence. *NASA TM*103926.

NYGAARD, K. J. & GLEZER, A. 1991 Evolution of streamwise vortices and generation of small-scale motion in a plane mixing layer. *J. Fluid Mech.* **231**, 257 301.

OSTER, D. & WYGNANSKI, I. 1982 The forced mixing layer between parallel streams. *J. Fluid Mech.* **123**, 91–130.

PIERREHUMBERT, R. T. & WIDNALL, S. E. 1982 The two- and three-dimensional instabilities of a spatially periodic shear layer. *J. Fluid Mech.* **114**, 59–82.

RILEY, J. J. & METCALFE, R. W. 1980 Direct numerical simulation of a perturbed turbulent mixing layer. *AIAA Paper* 80-0274.

ROGERS, M. M. & MOSER, R. D. 1991 The three-dimensional evolution of a plane mixing layer Part 1. The Kelvin–Helmholtz roll-up. *NASA TM*103856.

ROGERS, M. M. & MOSER, R. D. 1992 The three-dimensional evolution of a plane mixing layer: the Kelvin–Helmholtz rollup. *J. Fluid Mech.* **243**, 183–226 (referred to herein as RM).

ROGERS, M. M. & MOSER, R. D. 1993 Spanwise scale selection in plane mixing layers. *J. Fluid Mech.* **247**, 321–337.

SPALART, P. R., MOSER, R. D. & ROGERS, M. M. 1991 Spectral methods for the Navier–Stokes equations with one infinite and two periodic directions. *J. Comput. Phys.* **96**, 297–324.

STUART, J. T. 1967 On finite amplitude oscillations in laminar mixing layers. *J. Fluid Mech.* **29**, 417–440.

TOOR, H. L. 1962 Mass transfer in dilute turbulent and non-turbulent systems with rapid irreversible reactions and equal diffusivities. *AIChE J.* **8**, 70–78.

WINANT, C. D. & BROWAND, F. K. 1974 Vortex pairing: the mechanism of turbulent mixing-layer growth at moderate Reynolds number. *J. Fluid Mech.* **63**, 237–255.

YANG, Z. & KARLSSON, S. K. F. 1991 Evolution of coherent structures in a plane shear layer. *Phys. Fluids* A **3**, 2207–2219.

ZELDOVICH, Y. B. 1951 On the theory of combustion of initially unmixed gases. *NACA TM*1296.